J Ther Eng, Vol. 12, No. 2, pp. 610−634, March, 2026

Journal of Thermal Engineering
Web page info: https://jten.yildiz.edu.tr
DOI: 10.14744/thermal.0001104

Research Article

Water heater employing granular coal photothermal absorber and solar thermal collector combination

Alfan SARIFUDIN[1,2,*], Indri YANINGSIH[3], Budi KRISTIAWAN[3], Aditya WIBAWA[4], Ahmad FUDHOLI[5,6], Muhammad AZIZ[7,8]

[1]*Department of Computer Engineering, Automotive and Robotics Program, BINUS ASO School of Engineering, Bina Nusantara University, Jakarta, 15143, Indonesia*
[2]*Department of Industrial Engineering, Automotive and Robotics Program, , BINUS ASO School of Engineering, Bina Nusantara University, Jakarta, 15143, Indonesia*
[3]*Department of Mechanical Engineering, Universitas Sebelas Maret, Indonesia*
[4]*Research Center for Geological Resources, National Research and Innovation Agency (Badan Riset dan Inovasi Nasional / BRIN), 57126, Indonesia*
[5]*Solar Energy Research Institute, Universiti Kebangsaan Malaysia, Selangor, 43600, Malaysia*
[6]*Center for Energy Conversion and Conservation, National Research and Innovation Agency (Badan Riset dan Inovasi Nasional / BRIN), 15310, Indonesia*
[7]*Department of Mechanical Engineering, The University of Tokyo, Tokyo, 113-8656, Japan*
[8]*Institute of Industrial Science, The University of Tokyo, Tokyo, 113-8656, Japan*

ARTICLE INFO

Article history
Received: 07 January 2025
Revised: 30 April 2025
Accepted: 06 May 2025

Keywords:
Differential Scanning Calorimetry (DSC); Renewable Energy; Solar Energy; Spectrophotometry; Thermogravimetric Analysis (TGA); Thermodynamic

ABSTRACT

Coal's conventional use causes environmental problems and threatens future energy security. This research presents a photothermal method for coal use, integrating a granular coal photothermal absorber into a solar thermal collector for solar water heater. This method offers a novelty in utilizing heat energy from coal, which is usually burned coal, but this photothermal method converts light into heat. Therefore, the photothermal method will not produce emissions and can be used repeatedly. The solar thermal collector combines a Fresnel lens and a parabolic reflector. Scanning electron microscope and energy dispersive spectroscopy analysis shows the granular coal photothermal absorber's light-trapping carbon structure, with optimal sizes of 10-20 mesh generating temperatures of 378.15 K and an absorbance of 1.04. Thermogravimetric analysis and differential scanning calorimetry reveal a working temperature range of 336.31–684.31 K, with an optimal light-to-heat conversion temperature of 399.25 K, achieving 86.64% energy efficiency and 21.29% exergy efficiency. Performance tests show optimal solar water heater storage temperatures of 317.88 K and 316.75 K. The water temperature in the storage corresponds to the application of warm water bathing. The solar thermal collector's maximum energy and exergy efficiencies are 33.06% and 5.51%, respectively, with average efficiencies of 22.90% and 3.44%. The solar water heater system peaks at 27.85% energy and 5.90% exergy efficiency, with average efficiencies of 20% and 3.09%. This approach highlights potential sustainable energy use and reduced environmental impacts of coal utilization.

Cite this article as: Sarifudin A, Yaningsih I, Kristiawan B, WibawaA, Fudholi A, Aziz M. Water heater employing granular coal photothermal absorber and solar thermal collector combination. J Ther Eng 2026;12(2):610−634.

***Corresponding author.**
*E-mail address: alfansarifudin.indonesia@gmail.com, alfan.sarifudin@binus.edu

This paper was recommended for publication in revised form by Editor-in Chief Ahmet Selim Dalkilic

INTRODUCTION

Coal is one of the most abundant natural rocks and is currently the most widely used energy source worldwide. In 2023, the coal supply reached 156,636,851 TJ, which is equivalent to 27% of the world's energy supply, and its dominant supply is only below oil at 29% [1]. Currently, the most popular method for utilizing the energy contained in coal is combustion [2]. However, coal combustion has the negative effect of releasing carbon emissions into the atmosphere, damaging the environment [3]. In addition, coal combustion also faces concerns due to its limited resources and non-renewable (non-renewable). In response to these problems, utilizing coal without burning is considered an appropriate option. It includes the photothermal process, where coal is used as a light absorber to convert solar radiation into heat. This concept is promising because solar energy is renewable with abundant availability, although its utilization is still very low. The potential of solar energy reaching Earth reaches about 440,000 TWh [4]. However, the use of solar energy is still low because, by 2022, it will only be 1,322.62 TWh or less than 1% of the global energy mix and its potential [5], [6].

Coal is a sedimentary rock whose primary composition element is carbon. He et al. [7] have classified various carbon-based materials as photothermal absorbers. Therefore, converting solar radiation energy into heat via a photothermal method is more prospective for sustainability and protecting the environment than just burning it. Moreover, several previous studies have proven that natural rocks with a granular structure are useful as photothermal absorbers in various types of solar thermal collectors and applications. Natural materials with dark colors and pores have the potential to produce reliable photothermal performance for low and medium temperatures such as solar water heaters [8]. The granular structure is a type of light trap structure that can increase light absorbance because it recaptures the reflected light [9]. Table 1 presents the latest research developments regarding solar photothermal absorbers with granular structures from natural rock materials.

Solar thermal performance is also greatly influenced by the type of its collector [21]. Most of the previous research presented in Table 1 used a flat plate type. Therefore, the temperature generation performance was relatively low. Based on the classification carried out by Bie et al. [22], solar thermal collector (STC) temperatures are classified into low (<353.15 K), intermediate (353.15 K to 523.15 K), and high (>523.15K). The low-temperature generation by flat plate is because the concentration ratio is ≤1 times [23]. The experiment conducted by Elmaadawy et al. [18] using a parabolic reflector tracking system (PRTC) could be classified as an intermediate temperature. It is because the PRTF's temperature could reach a temperature of 375.15 K [16]. This happens because the concentration of the parabolic reflector is 15-40 times higher than the flat plate type [24].

As shown in Table 1, it can be understood that there has been no research using coal as a photothermal absorber material for solar thermal collectors. The latest research conducted by Sarifudin et al. [25], who compared natural

Table 1. Development of research on solar photothermal absorbers with granular structures from natural rock materials

Materials	Application	Type of Collectors	Performance			Ref.
			α	T	η	
Pebble	Solar water heater	Flat plate	Na	336.95 K	86.40%	[10]
Granit	Solar water heater	Flat plate	Na	ΔT 7.64 K	64.44%	[11]
Gravel	Solar dryer	Flat plate	Na	332.45 K	50.12%	[12]
Pumice-carbon-silver	Solar steam generation and water treatment	Prismatic	94,9%	<318.15 K	88,80%	[13]
Pumice	Solar desalination	Flat plate	Na	≈343.15 K	28.80%	[14]
Gravel	Solar desalination	Hemispherical	Na	342.15 K	65.68%	[15]
Gravel	Solar desalination	Parabolic concentrator solar tracking system	Na	375.15 K	41.83%	[16]
Gravel - limestone (composite)	Solar air heater	Flat plate	93,5%	333.15 to 343.15 K	10%	[17]
Gravel, wick, and carbon black nanoparticles	Solar desalination	Flat plate	Na	344.15 K	50%	[18]
Fine stone (black basalt)	Solar desalination	Flat plate	Na	335.25 K	32.07%	[19]
Pebbles	Solar desalination	Flat plate	Na	332.15 K	44%	[20]

*Note: α is the light absorbance of the photothermal absorber, η is the efficiency of the solar collector system, and T is the temperature of the absorber or the material heated by the absorber.

rocks with the granular structure of andesite, coal, and pumice using controlled laboratory experimental methods, found that coal material was the best. Furthermore, tests using concentrated xenon light radiation in laboratory scale condition showed better heat generation performance than direct radiation [26]. Therefore, the next urgency is to know coal material as a photothermal absorber which is installed in concentrated solar collectors. Moreover, this research also tested the optimal granular size and operational limits.

The novelty of this research is in the utilizing a different design type of STC. A type of STC with an equivalent concentration level is necessary to obtain a temperature generation comparable to the results of the research findings by Elmaadawy et al. [18]. Fresnel Lens is a type of solar collector with a concentration equivalent to a value of 15-40 times [27].

This research uses a stationary system to consider system simplification. The tracker system is more complicated because it requires an electrification device to control the automation system and drive motor. However, the stationary system has a weakness due to the sun's movement, so the light's focus cannot always be precisely on the absorber. Therefore, the Fresnel lens collector is combined with a compound parabolic reflector to reflect the unfocused light to the absorber. A compound parabolic reflector is a collector with an intermediate performance because its concentration reaches 1-5 times with an operational temperature range of 333.15 to 513.15 K [28]. Moreover, Fresnel lens collectors have the advantages of using little material, cost-effectiveness, and high optical efficiency [29].

Based on the background of the problems above and the solutions offered, this research aims to determine the morphology and element composition of a granular coal photothermal absorber (GCPA). Considering the research findings of Attia et al. [15] and Mohamed et al. [19], granular size influences performance. Therefore, this study also optimizes size for temperature generation and light absorbance. Furthermore, this study also wants to know the operating temperature limit of GCPA without damage and its enthalpies. Finally, this study calculates the efficiency of energy and exergy for the fundamental component of GCPA and the systems of STC and SWH.

MATERIALS AND METHODS

The main objectives of this research lay in the development of GCPA materials and the STC-SWH system. Therefore,

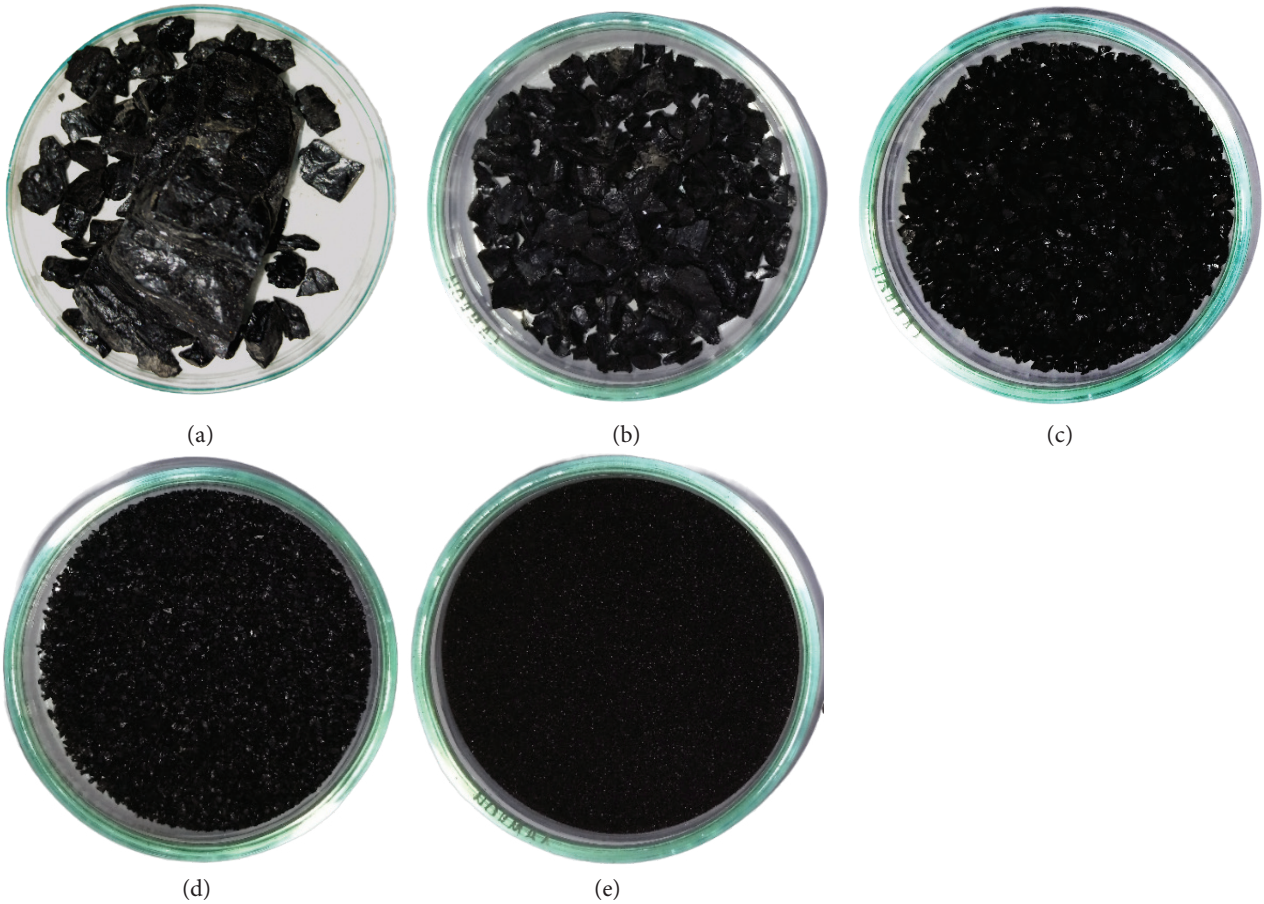

Figure 1. Granular coal in different sizes: (a) chunk, (b) 5−10 mesh, (c) 10−20 mesh, (d) 20−60 mesh, and (e) 60−100 mesh.

below is presented the process of making GCPA and the STC-SWH specifications that were researched and developed.

GCPA Preparation

The raw materials in this research are coal chunks with random sizes and dirty, as shown in Figure 1 (a). GCPA in various sizes that are ready to be tested are presented in Figure 1 (b)–(e). Specimens are prepared from coal chunks, which are then crushed [26]. The crushed materials are then sieved to pass through a big mesh and retained on a small mesh. Next, the sieve material is washed using water to obtain clean natural material. Washing not only removes dirt from the material but also removes fine grains that cover the pores of the material. The material that has been cleaned is then dried in an oven at 423.15 K for 3 h. After baking, the material is left in the open space for 48 h to make the temperature return to room temperature. The material preparation procedure is illustrated in Figure 2.

STC-SWH Specification

The STC-SWH tested in this study is presented in Figure 3(a), and its main components are presented in Figure 3(b). Moreover, the detailed information about each component is listed in Table 2.

Analytical Method

This study was conducted through a tiered experiment with a workflow shown in Figure 4. More detailed information regarding the analytical methods used is explained in each subchapter.

Scanning Electron Microscopy and Energy Dispersive Microscopy (SEM-EDS)

SEM test was carried out to determine the morphological properties of the material. Furthermore, the EDS test was used to determine the composition of the elements contained. Preparation is carried out with gold plating to ensure the GCPA structure does not burn easily during testing.

Temperature Generation in Simulator

The dried material was then tested for its temperature generation performance using a Fresnel lens collector under one solar illumination (1000 W/m^2). The power used by the xenon lamp is 100 W and 12 V DC voltage. The temperature generation test was conducted in a controlled room at a temperature of 298.15±1 K and humidity of 51.6 to 82.2 for 1200 s. The thermometer used has an accuracy of 0.25 K with a maximum error of ±2 K. The hygrometer used has an accuracy of 0.1% with a maximum error of ±3%. The 20 g of GCPA was tested in dry conditions.

Optical Analysis

Optical absorbance testing uses a spectrophotometer with a wavelength of 360–1100 nm (Vis-Infrared). Tests were carried out in dry conditions with all size variations. The purpose is to determine the optical properties of absorbance and transmittance of the material. Transmittance (%T) is defined as the amount of transmitted light (I) at each incident light wavelength (I_o), formulated in Eq. (1) [31], [32].

$$\%T = \frac{I}{I_o} \tag{1}$$

Meanwhile, absorbance (α_s) is defined as a logarithmic function formulated in Eq. (2) [33] or (3).

$$\alpha_s = \log_{10}\left(\frac{1}{\%T}\right) \tag{2}$$

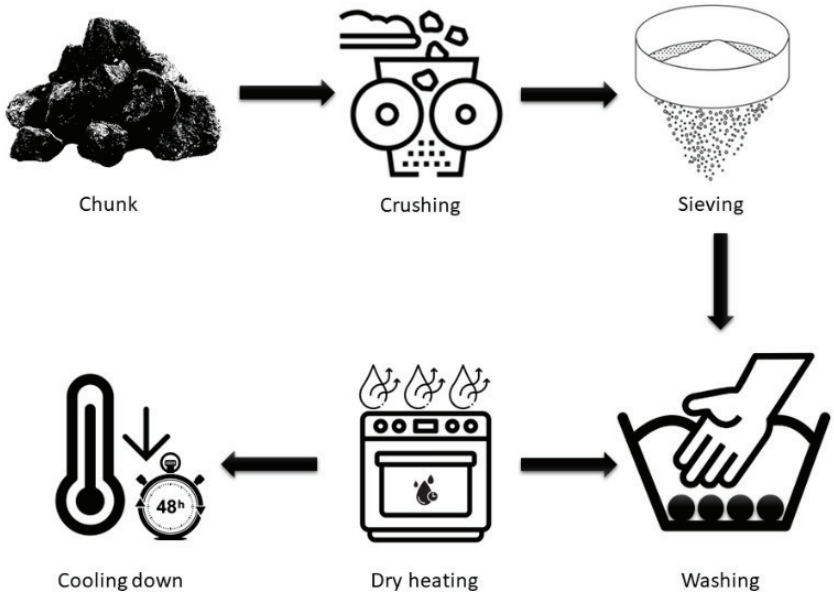

Figure 2. Material preparation process.

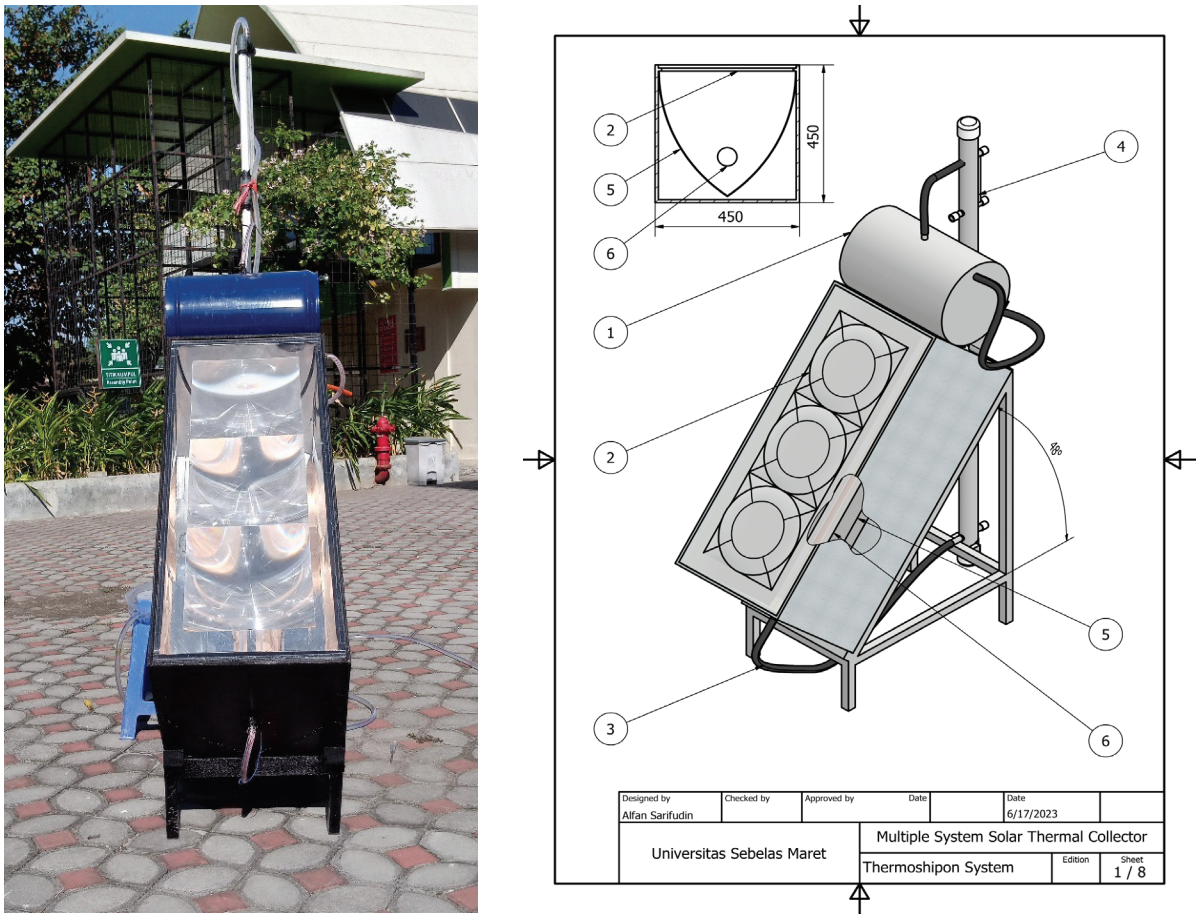

(a) (b)

Figure 3. Developed STC-SWH: (a) real view, and (b) main components illustration.

Table 2. Detail information of Figure 3 (b)

No.	Components	Specification
1.	Water tank	25 L or 23,325 kg of water
2.	Fresnel Lens	0.3 m × 0.3 m
3.	Plumbing	Insulator hose ¾ inch
4.	Water volume meter	1 mL
5.	Compound parabolic reflector	PVC mirror
6.	Tube receiver	48° (optimal angle) [30]. More detailed specifications are shown in Figure 5.

$$\alpha_s = \log_{10}\left(\frac{I_o}{I}\right) \tag{3}$$

To calculate the absorbance for all wavelengths is formulated in Eq. (4) [34].

$$\alpha = \frac{\int_{\lambda_{min}}^{\lambda_{max}} [1 - \%T(\lambda)] I_s(\lambda) d\lambda}{\int_{\lambda_{min}}^{\lambda_{max}} I_s(\lambda) d\lambda} \tag{4}$$

where λ_{max} is the maximum wavelength, and λ_{min} is the minimum wavelength. I_s is the wavelength resulting from the solar irradiation spectrum, and $T(\lambda)$ is the total transmittance at that wavelength (λ).

If the spectrophotometer machine directly displays absorbance and transmittance data at each wavelength, the absorbance and transmittance for all wavelengths are formulated in Eqs. (5) and (6).

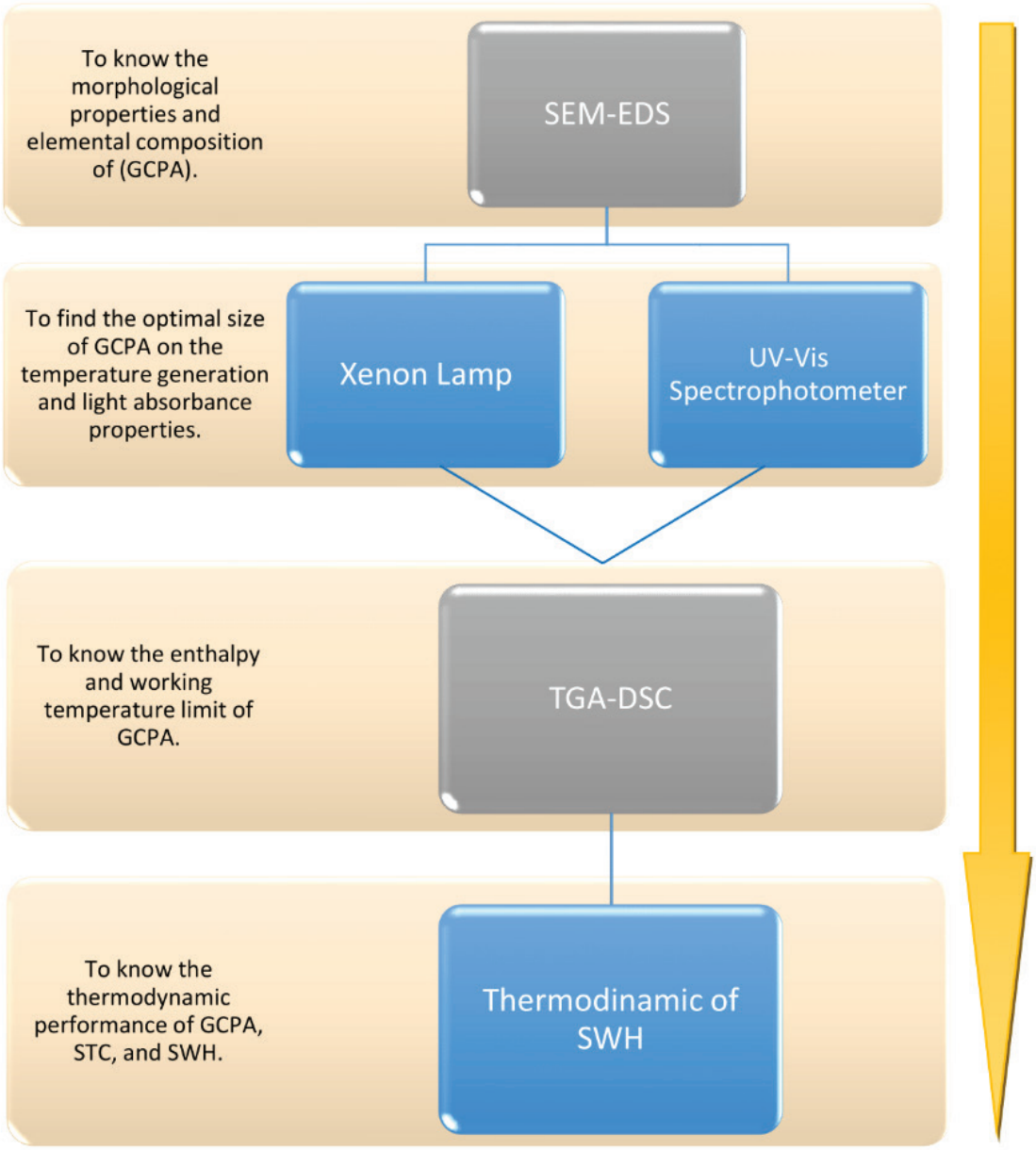

Figure 4. Workflow of the current research.

$$\alpha(\lambda) = \frac{\sum_{\lambda_{min}}^{\lambda_{max}} \alpha_s}{n} \quad (5)$$

$$\%T(\lambda) = \frac{\sum_{\lambda_{min}}^{\lambda_{max}} \%T}{n} \quad (6)$$

where n is the number of wavelength data taken.

TGA-DSC

Thermogravimetric analysis (TGA) testing is carried out to determine mass changes in the material because of thermal transition and degradation in the material. In this way, the working temperature operational limit of the photothermal absorber material will be known without significant damage. Furthermore, a differential scanning calorimetry (DSC) test is carried out to determine changes in material enthalpy due to physical and chemical degradation with changes in temperature at a certain time. These tests used granular coal material with optimal temperature generation and light absorbance performance. Apart from the fact that only material with the optimal size is selected in testing at STC-SWH, it is also because thermal degradation in coal is not influenced by particle size [35, 36]. Testing

was carried out, increasing the temperature by 1 K/min from 290.31 to 1,273.31 K.

Thermodynamics Analysis

The thermodynamic analysis is carried out in two conditions: unloaded and loaded conditions. Each test is carried out to determine the performance of the components (absorber) and main systems (STC and SWH). Unloaded condition testing is used to determine the GCPA performance in converting light to heat by temperature generation, energy efficiency, and exergy efficiency. The test was carried out on August 15-17 without being used to heat water. Meanwhile, the loaded condition test was carried out on August 12-14 to heat the water in the system. The position of each temperature sensor and the specifications of the components on the receiver tube are presented in Figure 5.

The loaded condition instrument was used to analyze the performance of the STC-SWH system. The sensor installation position in the system is presented in Figure 6.

The energy conversion efficiency ($\eta_{ece.abs}$) in the photothermal absorber is formulated by Yan and Li (2023) in Eq. (7).

$$\eta_{ece.abs} = \frac{m \times \Delta H_T}{I \times A_{abs} \times (\Delta t)} \quad (7)$$

where m is the mass of the absorber, ΔH_T is the change in enthalpy of the absorber at (T), I is the light illumination intensity, A_{abs} the surface area of the absorber exposed to radiation, and Δt is the time required to reach (T).

The measurements were carried out by Yan and Li (2023) in direct radiation conditions without being focused, whereas in this experimental case, the light was focused. Therefore, the focus value of the light radiation (F) is required, formulated in Eq. (8).

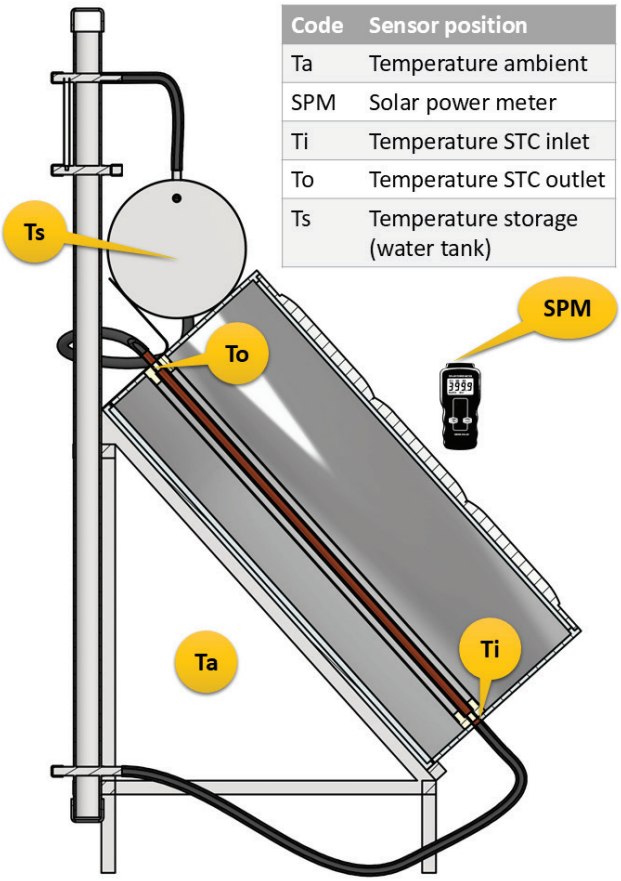

Figure 6. Sensor installation position for loaded condition test.

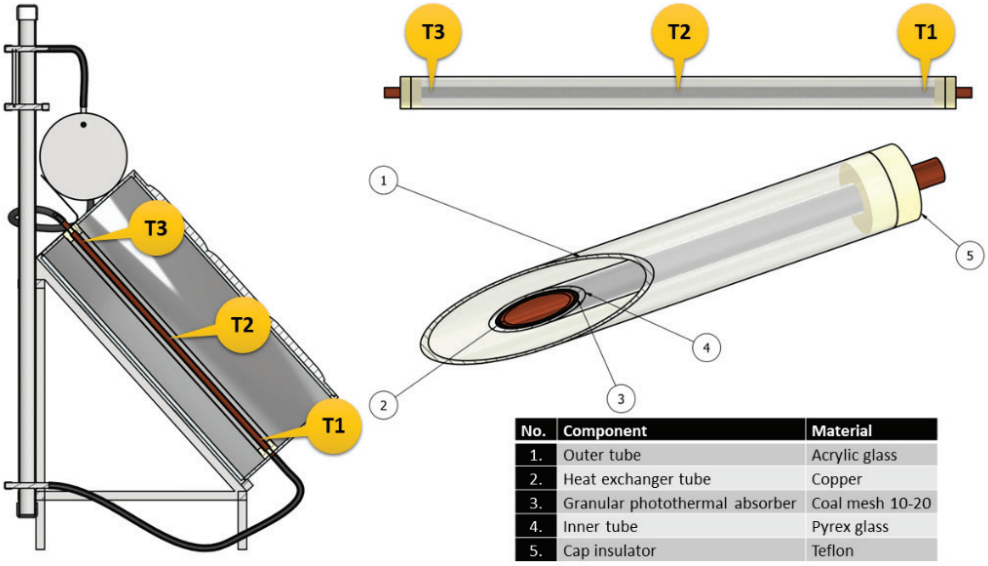

Figure 5. Installation position of the temperature sensor in the absorber and receiver components.

$$\eta_{abs} = \frac{m \times \Delta H_T}{F \times I \times A_{abs} \times (\Delta t)} \quad (8)$$

The radiation focus value (F) comes from the combined material transmittance (%T) and concentration ratio (C), formulated in Eq. (9).

$$F = \%T_{total} \times C \quad (9)$$

The concentration ratio factor (C) is the ratio of the lens surface area (A_{lens}) to the absorber surface area ($A_{absorber}$), formulated in Eq. (10) [37].

$$C = \frac{A_{lens}}{A_{absorber}} \quad (10)$$

The lens surface area in the simulation is 0.09 m^2 and the lens surface area in the SWH is 0.44 m^2. The absorber surface area in the simulator is 8.10×10^{-3} m^2 and the absorber surface area in SWH is 1.76×10^{-1} m^2.

The light that passes through a lens cannot be completely transmitted. Therefore, the transmittance of the system is the combination of several lenses' transmittance, which through the light passes, as formulated in Eq. (11).

$$\%T_{total} = \%T_1 \times \ldots \times \%T_n \quad (11)$$

The transmittance for the lens in the simulator is 92%, while the combined transmittance in the SWH is 0.73%. The transmittance of SWH is smaller than that of the simulator transmittance because the lens on the SWH is thicker and composed of two layers of sandwich (acrylic lens, Frensnel lens, and glass tube). The lens on the simulator only consists of a Fresnel lens. In addition, the SWH testing conditions are in a real environment, so there is dust that can reduce transmittance, while the simulator is placed in a closed room. The transmittance value is calculated using equation 11 and measured by comparing the intensity of light illumination transmitted by the lens to the intensity of light illumination on the lens surface.

Eqs. (7) to (11) can be simplified and Eq. (12) can be obtained.

$$\eta_{energy.abs} = \frac{m \times \Delta H_{(t,m,T)}}{\%T_{total} \times A_{lens} \times I \times (\Delta t)} \quad (12)$$

The exergy efficiency of the photothermal absorber is the ratio between the heat exergy converted by the photothermal absorber to the maximum potential exergy obtained from the radiation source, formulated in Eq. (13).

$$\eta_{exergy.abs} = \frac{\dot{E}x_{abs.heat}}{\dot{E}x_{sources}} \quad (13)$$

The heat conversion exergy by a photothermal absorber was formulated by Li et al. (2023) and Hu et al. (2023) using the maximum possible limit approach for heat energy that can be utilized in the Carnot formula written in Eq. (14).

$$\dot{E}x_{abs.heat} = \dot{Q}_{abs}\left(1 - \frac{T_a}{T_{abs}}\right) \quad (14)$$

where $\dot{Q}_{abs}$ is the heat flow in the absorber, T_a is the ambient temperature, and T_{abs} is the absorber temperature.

The heat flow rate of the photothermal absorber is formulated in Eq. (15).

$$\dot{Q}_{abs} = \eta_{opt.abs} \times \dot{G}_{sources} \quad (15)$$

where $\eta_{opt.abs}$ is the optimal energy efficiency and $\dot{G}_{sources}$ is the rate of solar radiation energy.

Exergy produced from light radiation sources ($\dot{E}x_{sources}$) is formulated using the Petela equation which is formulated in Eq. (16) [39].

$$\dot{E}x_{sources} = A_{abs} \times I_{sources}\left[1 + \frac{1}{3}\left(\frac{T_a}{T_{sources}}\right)^4 - \frac{4}{3}\left(\frac{T_a}{T_{sources}}\right)\right] \quad (16)$$

where A_{abs} is the surface area of the absorber, $I_{sources}$ is the intensity of the light radiation source, T_a is the ambient temperature, and $T_{sources}$ is the temperature of the light radiation source. The temperature of the arc of light in a xenon lamp is 1280.15 K [40], and the surface temperature of the sun is 6,273.15 to 20,273.15 K [41].

Based on the explanation of Eqs. (13) to (16), the exergy efficiency of the photothermal absorber can be simplified to Eq. (17).

$$\eta_{exergy.abs} = \frac{\eta_{opt.abs}\left(1 - \frac{T_a}{T_{sources}}\right)}{\left[1 + \frac{1}{3}\left(\frac{T_a}{T_{sources}}\right)^4 - \frac{4}{3}\left(\frac{T_a}{T_{sources}}\right)\right]} \quad (17)$$

Solar thermal collector energy efficiency ($\eta_{energy\ STC}$) is the ratio of the energy produced to the energy required to operate the system in Eq. (18) [42]. Where the energy produced is in the form of heat [43] and the energy input is in the form of solar radiation [44].

$$\eta_{energy\ STC} = \frac{\dot{E}_{output}}{\dot{E}_{input}} = \frac{\dot{E}_{useful\ heat}}{\dot{E}_{solar\ radiation}} = \frac{\dot{Q}}{\dot{G}} \quad (18)$$

Useful energy in the heat form ($\dot{E}_{heat}$) [45] or heat flowing in the pipe of STC ($\dot{Q}_{heat\ flow}$) [46] is formulated in Eq. (19).

$$\begin{aligned} \dot{E}_{useful\ heat} &= \dot{Q}_{heat\ flow.STC\ to\ WT} \\ &= Cp \times \dot{m} \times \left(T_{out(col)} - T_{in(col)}\right) \end{aligned} \quad (19)$$

In the thermosiphon mechanism, the mass flow rate of water ($\dot{m}$) is very slow, so it is difficult to measure. However, by the second law of the thermodynamics approach, which states that heat flows from high potential to low potential, the mass flow rate can be calculated. Evidence of mass flow in the system is a change in temperature increase in the storage even though the connecting hose between the STC outlet and storage inlet is an insulator, so the heat flow is convection. Finally, the system will go to the Zeroth law of thermodynamics (energy balance), which is formulated in Eq. (20).

$$\dot{Q}_{heat\ flow.STC\ to\ WT} \approx \dot{Q}_{haet\ change.wt} + \dot{Q}_{haet\ change.stc} + \dot{Q}_{heat\ flow\ loss.wt} + \dot{Q}_{heat\ flow\ loss.STC} \quad (20)$$

The water heat change rate in the tank is formulated in Eqs. (21) and (22) [47].

$$\Delta\dot{Q}_{heat\ change.wt} = \frac{\overline{Cp}_{water} \times m_{water\ in\ tank} \times \Delta T_{water\ in\ tank}}{\Delta t} \quad (21)$$

$$\Delta\dot{Q}_{heat\ change.wt} = \frac{\overline{Cp}_{water} \times m_{water\ in\ tank} \times (T_{tn} - T_{tn-1})}{\Delta t} \quad (22)$$

The water heat change rate in the STC is formulated in Eqs. (23) and (24).

$$\Delta\dot{Q}_{heat\ change.STC} = \frac{\overline{Cp}_{water} \times m_{water\ in\ STC} \times \Delta T_{water\ in\ STC}}{\Delta t} \quad (23)$$

$$\Delta\dot{Q}_{heat\ change.STC} = \frac{\overline{Cp}_{water} \times m_{water\ in\ STC} \times \frac{((T_{outlet} + T_{intlet})_{Tn} - (T_{outlet} + T_{intlet})_{tn-1})}{2}}{\Delta t} \quad (24)$$

where T_{tn} is the temperature in the n^{th} period and T_{tn-1} is the temperature in the previous period.

Considering that the value of Cp_{water} changes for changes in temperature, the average value in the range of temperature changes is used, formulated in Eq. (25).

$$\overline{Cp}_{water} = \left| \frac{Cp_{water.T_{t1}} + Cp_{waterT_{t2}}}{2} \right| \quad (25)$$

The water mass in the full tank and STC is 23.325 and 0.094 kg, respectively. Evaporation and condensation that occur do not change the mass significantly because the installed measuring instrument does not detect any changes in water volume.

Heat flow loss in the water tank ($\dot{Q}_{heat\ flow\ lost.wt}$) is calculated using Newton's law of cooling in Eq. 26, where k is the heat transfer coefficient and T_t is the temperature at the time (t) [48].

$$\frac{dQ}{dt} = k(T_{ambient} - T_t) \quad (26)$$

For application in this case study, Eq. 26 can be written as Eq. (27).

$$\dot{Q}_{heat\ flow\ loss.wt} = k(T_{ambient} - T_t) \quad (27)$$

When solar radiation power has a value of 0, no heat energy from solar radiation conversion enters the water tank, so the heat energy change rate in the tank is the heat loss rate, as formulated in Eq. (28).

$$\frac{\Delta Q_{heat\ flow\ loss.wt}}{\Delta t} = k(T_{ambient} - T_t) \quad (28)$$

The heat loss rate at the collector is also formulated similarly in Eq. (29).

$$\frac{\Delta Q_{heat\ flow\ loss.STC}}{\Delta t} = k(T_{ambient} - T_t) \quad (29)$$

Based on calculations of the temperature data of the system in Figure 13 using Eqs. (28) and (29), the k value in the water tank was found to be -3,844 J/s·K while at the collector, it was -0,086 J/s·K.

The K value validation is carried out using the Zeroth law of thermodynamics (energy balance between systems), which applies Eq. (30).

$$\begin{aligned} \dot{Q}_{heat\ flow.STC\ to\ WT} &\approx \dot{Q}_{haet\ change.wt} + \dot{Q}_{haet\ change.stc} \\ &+ \dot{Q}_{heat\ flow\ loss.wt} + \dot{Q}_{heat\ flow\ loss.STC} \\ &\approx \overline{Cp} \times \dot{m} \times (T_{out(col)} - T_{in(col)}) \end{aligned} \quad (30)$$

The validation test of each calculation in Eq. (30) using the coefficient of variation shows that the error level is 0%. The calculation results are presented in Figure 14.

Energy input ($\dot{E}_{input}$) per unit time is formulated in Eq. (31) [49], where I_s is the solar intensity and A_{STC} is the STC surface area. The conservation of energy in terms of the first law of thermodynamics (energy cannot be created or destroyed but can change form) is formulated in Eq. (31). Where the input energy ($\dot{E}_{input}$) turns into useful energy in the form of heat ($\dot{E}_{useful\ energy\ (heat)}$) and useless energy ($\dot{E}_{useless\ energy}$).

$$\begin{aligned} \dot{E}_{input} &= \dot{E}_{solar\ radiation} = \dot{G} \\ &= I_s \times A_{STC} \rightarrow \dot{E}_{useful\ energy\ (heat)} \\ &+ \dot{E}_{useless\ energy} \end{aligned} \quad (31)$$

Useless energy is formed due to the apparent motion of the sun and errors in collector geometry, which result in the focus of light not being able to fall precisely on the absorber. Furthermore, useless energy occurs because there is light that is reflected and transmitted by the collector and absorber. Useless energy is also caused by absorber conversion inefficiencies. Therefore, the absorber cannot convert all the sunlight obtained as formulated in Eq. (32).

$$\dot{E}_{useless\ energy} = \dot{G}_{unfocused} + \dot{G}_{reflectance} + \dot{G}_{transmittance} + \dot{E}_{inefficiencies.abs} \quad (32)$$

The contribution of useless energy ($\%\dot{E}_{useless\ energy}$) to STC is formulated in Eq. (33).

$$\%\dot{E}_{useless\ energy} = \frac{\dot{E}_{useless\ energy}}{\dot{E}_{input}} = \frac{\dot{E}_{useless\ energy}}{\dot{E}_{solar\ radiation}} \quad (33)$$

Eqs. (32) and (33) are too complicated because it requires measuring many parameters, so $\%\dot{E}_{useless\ energy}$ is calculated using the simpler formula in Eq. (34).

$$\%\dot{E}_{useless\ energy} = 1 - \eta_{energy.STC} \quad (34)$$

The exergy balance at STC is formulated in Eq. 35 [50], [51].

$$\dot{E}x_{inlet} - \dot{E}x_{outlet} = \dot{E}x_{destruction} \quad (35)$$

where $\dot{E}x_{inlet}$ is the exergy rate at the inlet, $\dot{E}x_{destruction}$ is the exergy rate of destruction, and $\dot{E}x_{outlet}$ is the exergy rate at the outlet.

Next, each exergy rate is formulated following Eqs. (36) and (37) [52].

$$\dot{E}x_{inlet} = \dot{m} \times \overline{Cp} \times \left\{(T_{inlet} - T_0) - T_0 \times ln\left(\frac{T_{inlet}}{T_0}\right)\right\} \quad (36)$$

$$\dot{E}x_{outlet} = \dot{m} \times \overline{Cp} \times \left\{(T_{outlet} - T_0) - T_0 \times ln\left(\frac{T_{outlet}}{T_0}\right)\right\} \quad (37)$$

where $\dot{m}$ is water's mass flow rate, Cp is water's specific heat coefficient, T_{inlet} is the temperature at the inlet, T_0 is the ambient temperature, and T_{outlet} is the temperature at the outlet. The mass flow rate of water in the thermosiphon mechanism is difficult to measure because it is very slow. The solution, mass flow rate is calculated using Eqs. (38) and (39).

$$\dot{Q}_{heat\ flow.STC\ to\ WT} = \overline{Cp} \times \dot{m} \times \left(T_{outlet(STC)} - T_{inlet(STC)}\right) \quad (38)$$

$$\dot{m} = \frac{\dot{Q}_{heat\ flow.STC\ to\ WT}}{\overline{Cp} \times \left(T_{outlet(STC)} - T_{inlet(STC)}\right)} \quad (39)$$

Exergy efficiency in STC is formulated as the increase in exergy between the inlet and outlet flow relative to the input exergy [53]. Therefore, exergy efficiency is formulated as useful exergy relative to exergy from solar radiation in Eq. 40 [54].

$$\eta_{exergy\ STC} = \frac{\dot{E}x_{outlet} - \dot{E}x_{inlet}}{\dot{E}x_{input}} = \frac{\dot{E}x_{useful}}{\dot{E}x_{\dot{G}}} \quad (40)$$

Exergy input ($\dot{E}x_{input}$) from solar radiation is formulated in Eq. 41 [54].

$$\dot{E}x_{input} = \dot{E}x_{\dot{G}} = \bar{I}_{solar} \times A_{collector} \times \left[1 + \left\{\frac{1}{3}\left(\frac{T_0}{T_s}\right)^4\right\} - \left\{\frac{4}{3}\left(\frac{T_0}{T_s}\right)\right\}\right] \quad (41)$$

where $\bar{I}_{solar}$ is the solar intensity, $A_{collector}$ is the collector surface area, and T_s is the solar surface temperature.

Next, the sustainability index (SI) is calculated in Eq. (42), which is a crucial exergy-based effectiveness parameter [55].

$$SI_{SWH} = \frac{1}{1 - \eta_{exergy.SWH}} \quad (42)$$

SWH energy efficiency (η_{SWH}) [56] or charging efficiency [57] is defined as the ratio of heat energy stored as hot water in the tank to solar radiation energy formulated in Eq. (43). Therefore, SWH energy efficiency can be interpreted as the efficiency of storing heat energy in the SWH system.

$$\eta_{energy.SWH} = \frac{E_{saved}}{E_{input}} = \frac{E_{heat\ water\ tank}}{E_{solar\ radiation}} = \frac{Q_{water\ in\ tank}}{G_{cumulative}} \quad (43)$$

where the amount of heat in the tank ($Q_{water\ in\ tank}$) is formulated in Eq. (44) [58], [59], [60] and $G_{cumulative}$ is formulated in Eq. (45) [61].

$$Q_{water\ in\ tank} = cp \times m \times (T_{tn} - T_0) \quad (44)$$

$$G_{cumulative} = A_{collector} \int_{t0}^{tn} I_s(t)\, dt \quad (45)$$

where cp is the specific heat coefficient of water, m is the mass of water, T_{tn} is the temperature at time t, and T_0 is the initial temperature. Then, $A_{collector}$ is the collector's surface area, I_s is the solar intensity, and t is the duration of exposure.

As the first law of thermodynamics, energy conservation in SWH satisfies Eq. (46), where the total energy input is converted to the total saved and unsaved energy.

$$\sum E_{input} = \sum E_{saved} + \sum E_{not\ saved} \quad (46)$$

The total energy that cannot be stored is the accumulated useless energy and heat loss, formulated in Eq. (47).

$$\sum E_{not\ saved} = \sum E_{useless} + \sum E_{heat\ loss} \quad (47)$$

Exergy SWH compares exergy outcome to exergy input, formulated in Eq. (48) [62].

$$\eta_{exergy.SWH} = \frac{Exergy\ outcome}{Exergy\ input} \quad (48)$$

The outcome exergy is formulated using the Jeter equation because it comes from the heat source (photothermal absorber), as written in Eq. (49) [63].

$$Exergy\ outcome = Q_{water\ in\ tank} \times \left\{1 - \left(\frac{T_a}{T_s}\right)\right\} \quad (49)$$

where $Q_{water\ in\ tank}$ is the increase in heat stored in the water tank, T_a is the ambient temperature, and $T_{sources}$ is the temperature of the source (absorber).

Furthermore, the exergy input is the accumulated exergy of solar energy received by the STC, formulated using the Petela formula [39], which can be written as Eq. (50).

$$Exergy\ input = G_{cumulative} \times \left\{1 - \left(\frac{4}{3} \times \frac{T_a}{T_s}\right) + \left[\frac{1}{3} \times \left(\frac{T_a}{T_s}\right)^2\right]\right\} \quad (50)$$

Where $G_{cumulative}$ is the accumulated solar energy received by STC, T_a is the ambient temperature, and T_s is the source temperature (the sun's surface).

Uncertainty Analysis

To analyze uncertainty in experimental measurement data using Eq. (51), population deviation (σ), as used by Gitan and Al-Kayiem (2023).

$$\sigma = \sqrt{\frac{\sum(x_i - \bar{\mu})^2}{N}} \quad (51)$$

Meanwhile, the sample deviation (SD) can be calculated by using Eq. (52).

$$SD = \sqrt{\frac{\sum(x_i - \bar{x})^2}{N - 1}} \quad (52)$$

where x_i is the i value, $\bar{x}$ is the population mean, μ is the sample mean, and N is the population number.

Next, the uncertainty during measurement is represented as a coefficient of variation (CV), which is formulated in Eqs. (53) and (54).

$$\%CV_{population} = \frac{\sigma}{\bar{x}} \times 100\% \quad (53)$$

$$\%CV_{sample} = \frac{SD}{\bar{\mu}} \times 100\% \quad (54)$$

Considering that there are many variations in the sample in research, the formulation of the average CoV is for simplification in Eq. (55).

$$\%\overline{CV}_{sample} = \frac{\sum \%CV_{sample}}{n} \quad (55)$$

where n is the number of sample variations.

Uncertainty in performance is calculated using the error propagation equation (δ_l) formulated in Eq. (56) [65], [66], [67].

$$\delta_l = \sqrt{\delta_x^2 + \ldots + \delta_y^2} \quad (56)$$

RESULTS AND DISCUSSION

SEM-EDS

The SEM test with a magnification of 7,800 times in Figure 7 (a) shows that the material has a rough and crack gap structure like porous. The light trapping effect of the photothermal absorber to increase absorbance is caused by the presence of specific structures, including rough [68] and porous [69]. Therefore, the rough and crack gap structure of GCPA has a positive effect on temperature generation. These findings support the statement of Tuncer et al. [70] in his review study on carbon nanomaterial-based photothermal absorbers, that differences in particle size, shape, and concentration directly affect the thermal performance.

The EDS graph at three points is presented in Figure 7 (b), (c) and (d). This GCPA specimen is dominated by non-metal elements of carbon (C) and oxygen (O). The absence of the hydrogen element in the specimen indicates that the structure has changed to char. The release of H element bonds in coal is caused by baking during material preparation. The H element is released from the chemical structure of Carboxylic acid (C(=O)OH) because its decomposition temperature is only around 373.15 to 473.15 K [71]. However, it is also possible that hydrogen element is not found due to the inability of EDX to detect elements that have only one shell of K atoms, such as hydrogen and helium. The metal group elements aluminum (Al), iron (Fe), and niobium (Nb) contribute less than 5% based on mass concentration and less than 1% based on atomic concentration. The concentration contribution of each element in GCPA is presented in Table 3. The different elements composition of each coal do not indicate test inconsistencies, but different geological conditions of coal formation produce different element compositions [72].

Temperature Generation

The temperature generation test bar diagram in Figure 8 shows that a granular size of 10 to 20 mesh is optimal.

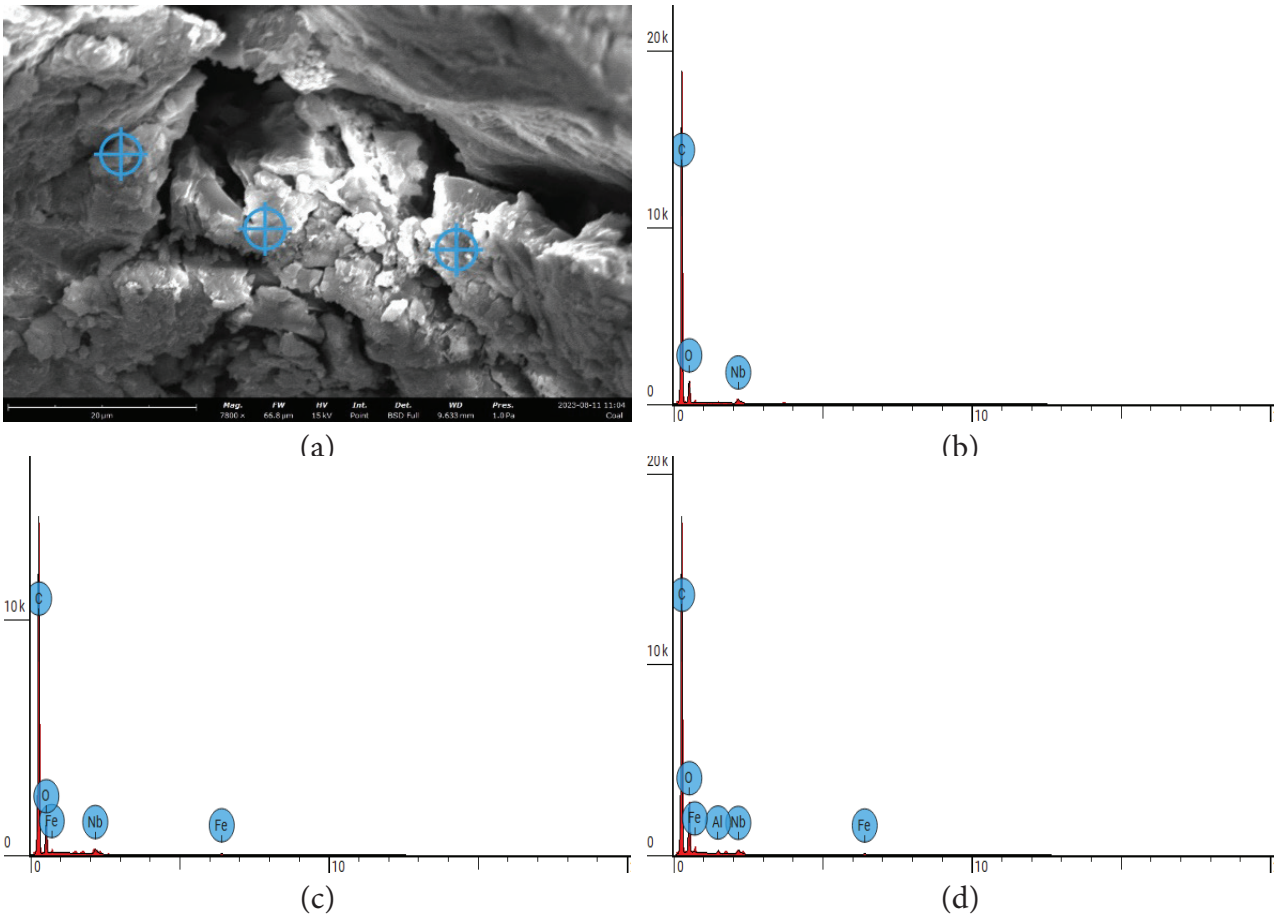

Figure 7. (a) SEM, (b) EDS graph spot 1, (c) EDS graph spot 2, and (d) EDS graph spot 3.

Table 3. Quantification of elements in GCPA

Position	Element			Concentration	
	Number	Symbol	Name	Atomic	Weight
Spot 1	6	C	Carbon	86.290%	80.619%
	8	O	Oxygen	13.323%	16.583%
	41	Nb	Niobium	0.387%	2.797%
Spot 2	6	C	Carbon	83.056%	75.479%
	8	O	Oxygen	16.003%	19.374%
	26	Fe	Iron	0.525%	2.221%
	41	Nb	Niobium	0.416%	2.926%
Spot 3	6	C	Carbon	78.073%	70.110%
	8	O	Oxygen	20.792%	24.875%
	13	Al	Aluminum	0.298%	0.602%
	26	Fe	Iron	0.504%	2.106%
	41	Nb	Niobium	0.332%	2.307%

There is a tendency that materials with higher absorbance will produce higher temperatures. The absorbance value of the material can be seen in Figure 9 (b) and Figure 10. However, other material properties such as thermal resistance, latent and sensible heat, hydrophilic–hydrophobic, and light-trapping capability can affect the temperature performance of photothermal absorbers [9]. The optimal granular photothermal absorber size and scale for each

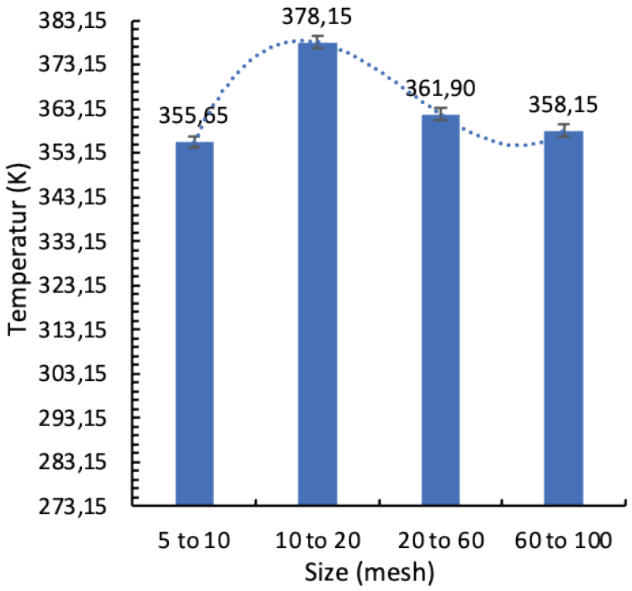

Figure 8. Temperature average of each GCPA size.

material can vary. Attia et al. [73], using granular gravel material from 4 to 16 mm, found the optimal size to be 16 mm. Meanwhile, Mohamed [19] used basalt stone 1 to 2 cm and found the optimal size to be 2 cm. Furthermore, the test used Au nanoparticles of 25 to 40 nm; the optimal size was 25 nm [74].

Optical Analysis

The transmittance and absorbance of each wavelength of light are presented in Figure 9. The light absorbance for all granular sizes tends to increase with an increasing wavelength of up to 910 nm. The optimal absorbance is in the infrared spectrum, with wavelengths from 700 to 910 nm. However, the transmittance increases after a wavelength of 910, and the absorbance decreases.

Figure 10 shows that the transmittance trend is inversely proportional to the temperature generation while the absorbance is directly proportional. Other research comparing different concentrations shows that materials with higher absorbance have higher temperature generation [75]. Anomalies appear in the size ranges of 40–60 and 60–100 but remain insignificant as they fall within overlapping measurement uncertainty limits. Therefore, determining the optimal material for a photothermal absorber is insufficient, as with one of the absorbance spectrophotometry or temperature generation tests using a lamp simulator. Based on the highest temperature generation test and the highest absorbance spectrophotometry test, it is known that the optimal granular size is mesh 10 to 20. The optimal mesh size confirms that the contact gaps between granules can trap light optimally and show a trend of higher absorbance, resulting in higher temperatures. The elemental concentrations in natural materials are generally less uniform than in purified materials, leading to more significant uncertainty in test results. Furthermore, the material's transmittance and absorbance values may be inconsistent due to the random arrangement of its granular structure, which leads to variations in the size of gaps acting as light traps. The SEM-EDS test data results in Figure 7 confirm the condition of non-uniformity of elemental composition and random gap size.

TGA-DSC

TGA-DSC testing on GCPA, which has a mesh size of 5-10, is presented in Figure 11 and is divided into four stages. The first stage is dehydration and desorption, starting from the beginning of the test, characterized by an endothermic reaction at a temperature of 290–336.31 K. In

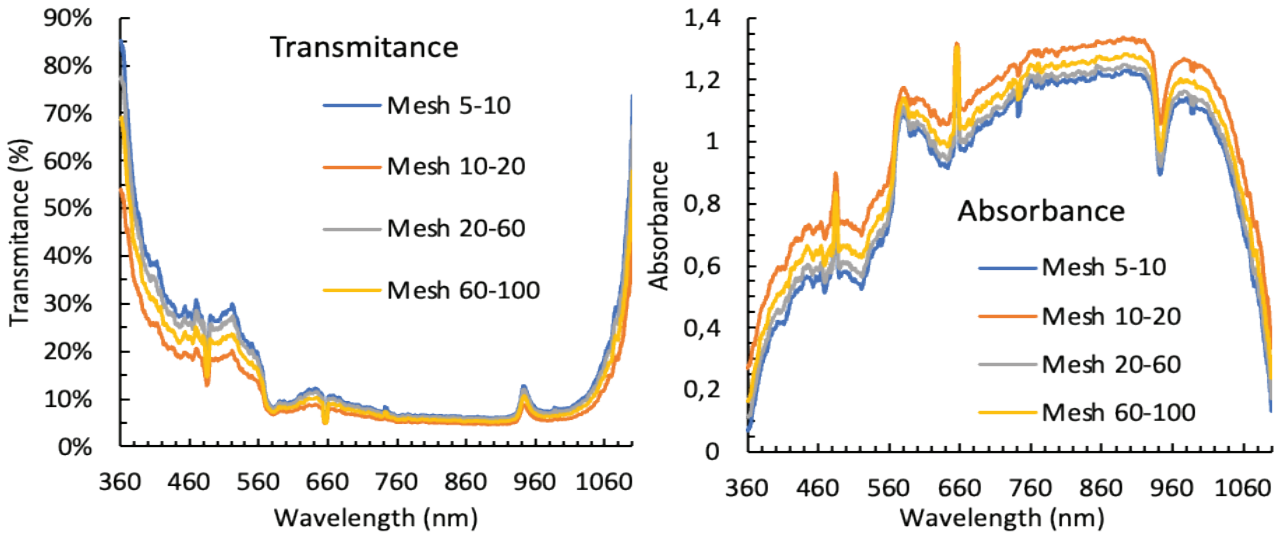

Figure 9. Optical properties (a) transmittance and (b) absorbance.

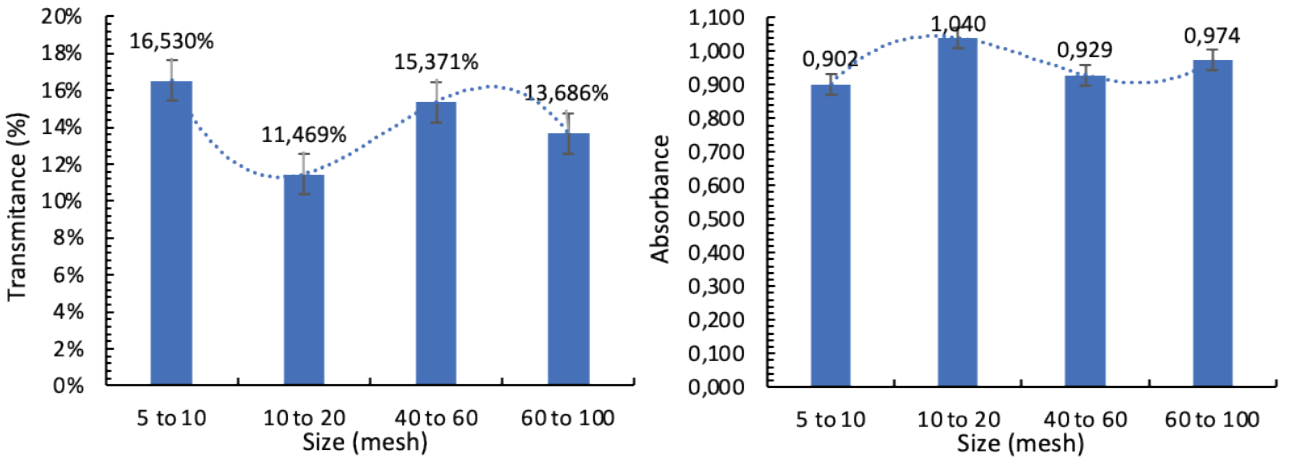

Figure 10. Optical properties throughout the wavelength (a) transmittance and (b) absorbance.

the first stage, an endothermic reaction occurs due to the removal of water vapor and gas desorption [76]. Next, the second stage begins when an exothermic reaction occurs at a temperature of 336.31-684.31 K with a mass change of 11.95%.

In the second stage, this is the ideal working temperature for the photothermal absorber because GCPA releases heat. Furthermore, there was no significant damage to the material in this area, as indicated by the lack of substantial change in mass. In the oxidation phase, the mass can increase or decrease depending on the major functional groups contained in the coal [76]. The increase in mass in coal samples is due to the presence of carboxyl groups (-COOH), which contribute to the increase in CO_2 gas and carbonyl groups (-C==O), which contribute to the increase in *CO* gas. Meanwhile, mass loss is caused by methyl groups ($-CH_3$) and methylene ($-CH_2-$).

The third stage (degradation) begins when the exothermic oxidation reaction ends, characterized by rapid mass changes due to pyrolysis and combustion reactions, depending on the availability of oxygen during the reaction. Mandal et al. [77] reported the degradation of combustion in Indian coal, and Kellali et al. [78] reported that the degradation of pyrolysis in lignite coal occurs exothermically and endothermically. In the degradation stage, the mass release is permanent; therefore, at this stage, the coal is considered

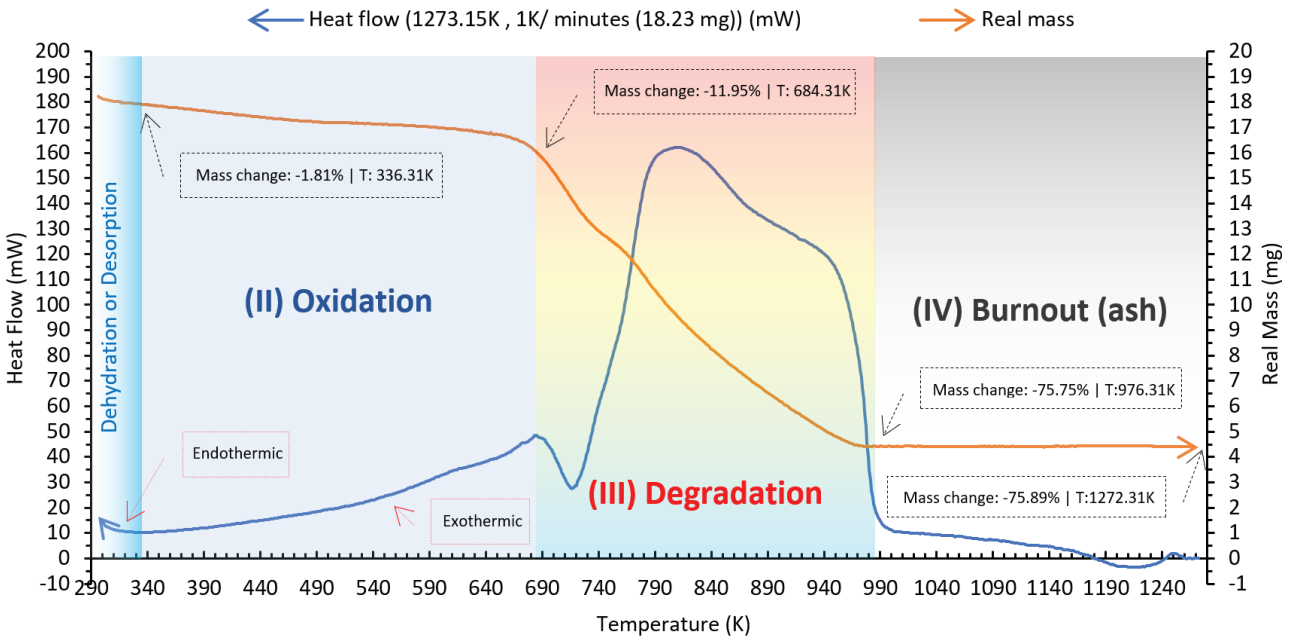

Figure 11. TGA-DSC of granular coal.

to have experienced structural damage as a photothermal absorber. The TGA test shows that the degradation stage starts at a temperature of around 684.31K, in Figure 11, while in the photothermal absorber test in the collector, the highest temperature is 399.25K, in Figure 12. These results show that the collector design is safe and does not cause damage because the generation temperature is still below the degradation temperature.

The degradation stage ends when the change in specimen mass begins to slope and begins to enter the burnout stage. In the burnout stage, the mass change is insignificant compared to the temperature change. The graphic data shows that heating with a temperature change reaching 296 K for 296 min only experienced a mass change of 0.14%, and ash contained in the GCPA is 24.11%. Furthermore, the visual characteristic that can be observed is that the specimen has turned to ash.

Thermodynamics Analysis

Temperature generation of GCPA

The results of testing the temperature generation of GCPA under real sunlight are presented in Figure 12. The highest light intensity during the test occurred at noon. Meanwhile, the highest GCPA temperature is at 1:00 PM for all sensor points. The maximum temperature in real testing was 399.25 K, so the results were higher than using a xenon lamp simulator of 378.15 K. This happens because the wavelength spectrum of sunlight is more diverse, the power intensity is higher, and the test duration is longer. Moreover, the direct test was carried out in a closed system (the absorber was in the receiver tube), while in the simulator, the absorber was tested in an open system (the absorber was on a petri dish). However, there is a possibility that the temperature generation in the simulator is higher than in the real test, depending on the different parameter conditions of each test.

Simulator testing and real testing are not intended to compare directly the two methods. Still, simulator testing is carried out as a guide to selecting the most optimal parameters (granular size) that will be tested in real conditions. This consideration is made because, in real testing, natural conditions cannot be controlled, and it can result in unreliable and biased data. As an alternative, comparative testing in real conditions must be carried out simultaneously using several collectors. However, the simultaneous method would be too expensive and impractical.

Energy and exergy efficiency of GCPA

The results of energy efficiency measurements for all GCPA size specimens and test conditions are presented in Table 4. A photothermal absorber with a higher temperature means a higher energy conversion efficiency.

The calculation results from Eq. (17) presented in

Table 5 show that exergy efficiency is lower than energy efficiency. Exergy can have a higher or lower value than

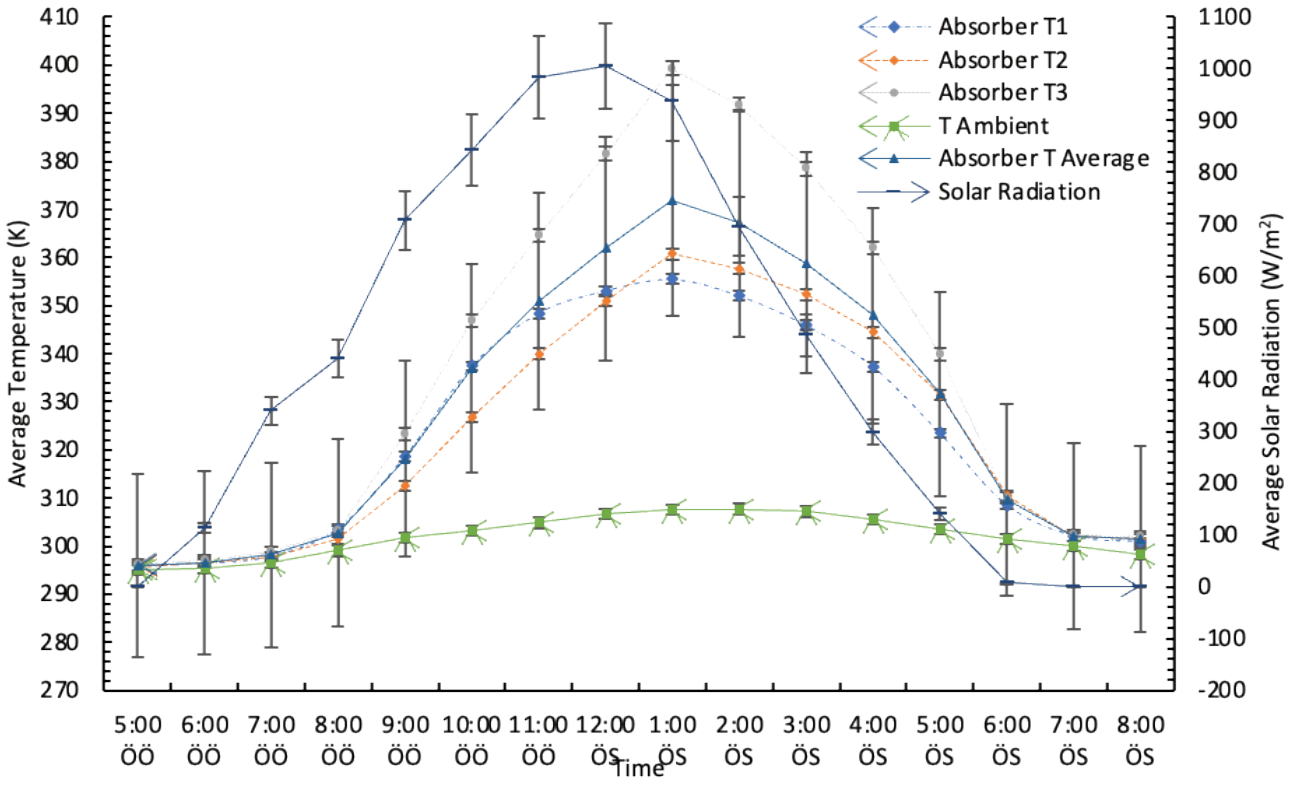

Figure 12. Temperature generation of absorbers in tube collector under unload condition.

Table 4. Energy conversion efficiency at all GPA sizes and test conditions

Radiation Source	Specimen (mesh)	m (Kg)	T_0 (K)	T_1 (K)	A_{lens} (m^2)	$\Delta H_{(t,m,T)}$ (W)	I (W/m^2)	$\%T_{total}$ (%)	Δt (s)	η_{abs} (%)
Xenon Lamp	5 to 10	0.02	298.15	355.65	0.09	1,791,263.38	1000.00	0.92	1800	24.04
	10 to 20	0.02	298.15	378.15	0.09	1,939,533.42	1000.00	0.92	1800	26.03
	20 to 60	0.02	298.15	361.90	0.09	1,820,620.96	1000.00	0.92	1800	24.43
	60 to 100	0.02	298.15	358.15	0.09	1,805,449.12	1000.00	0.92	1800	24.23
	100 to 200	0.02	298.15	344.40	0.09	1,740,111.86	1000.00	0.92	1800	23.35
Sun	10 to 20	0.24	296.12	399.25	0.44	33,574,316.06	1005.40	0.73	28800	86.64

Table 5. Efficiency Exergy Absorber

Radiation Sources	Specimen (mesh)	$\eta_{ece.abs}$ (%)	T_a (K)	T_{abs} (K)	$T_{sources}$ (K)	$\eta_{exergy.abs}$ (%)
Xenon lamp	5 to 10	24.04%	298.15	355.65	1,280.15	5.63%
	10 to 20	26.03%	298.15	378.15	1,280.15	7.97%
	40 to 60	24.43%	298.15	361.90	1,280.15	6.23%
	60 to 100	24.23%	298.15	358.15	1,280.15	5.88%
Sun	10 to 20	86.64%	307.57	399.25	6,273.15	21.29%

energy because exergy analysis reviews energy quality based on reference sources and the environment.

Temperature of system

The loaded condition test, in Figure 13, shows the highest intensity of solar radiation at 12.00. Meanwhile, the optimal temperature in the collector is reached at 2:00 PM, and the water in the storage is reached at 3:00 PM.This finding follows the trend conducted by Yanbolagh et al. [79], where the highest ambient temperature and water temperature in the collector occurred at 2:00 PM.The time shift to reach the optimal temperature in each component is closely related to the flow of energy and exergy in the system. Further discussion regarding this phenomenon is presented in the energy and exergy analysis of each system. Overall, the water storage temperature performance of SWH has met the needs

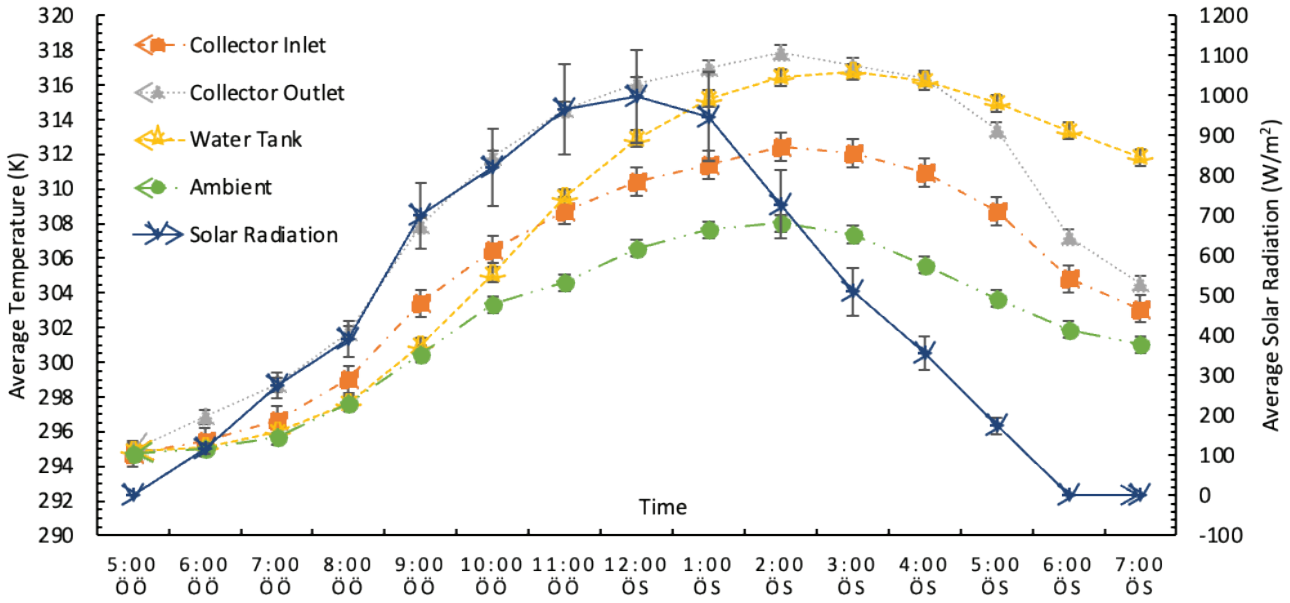

Figure 13. Temperature generation of STC-SWH system in load condition.

for warm water bathing in the range of 309.15 K to 318.15 K and generally ranges in 313.15 K [80].

Energy and exergy efficiency of STC

Figure 14 shows the energy flow rate in the STC and water tank (WT) systems. The positive heat change rate indicates that the system has increased storing heat. Meanwhile, the heat change rate is negative, indicating a decrease in stored heat which occurs starting between 3:00 PM. This condition occurs because the cooling heat rate release is faster than the heat that can be transferred from the photothermal absorber to the water working fluid.

Figure 16 shows that the highest STC energy efficiency occurs at 11:00 AM at 33.27%. After 11:00 AM, the

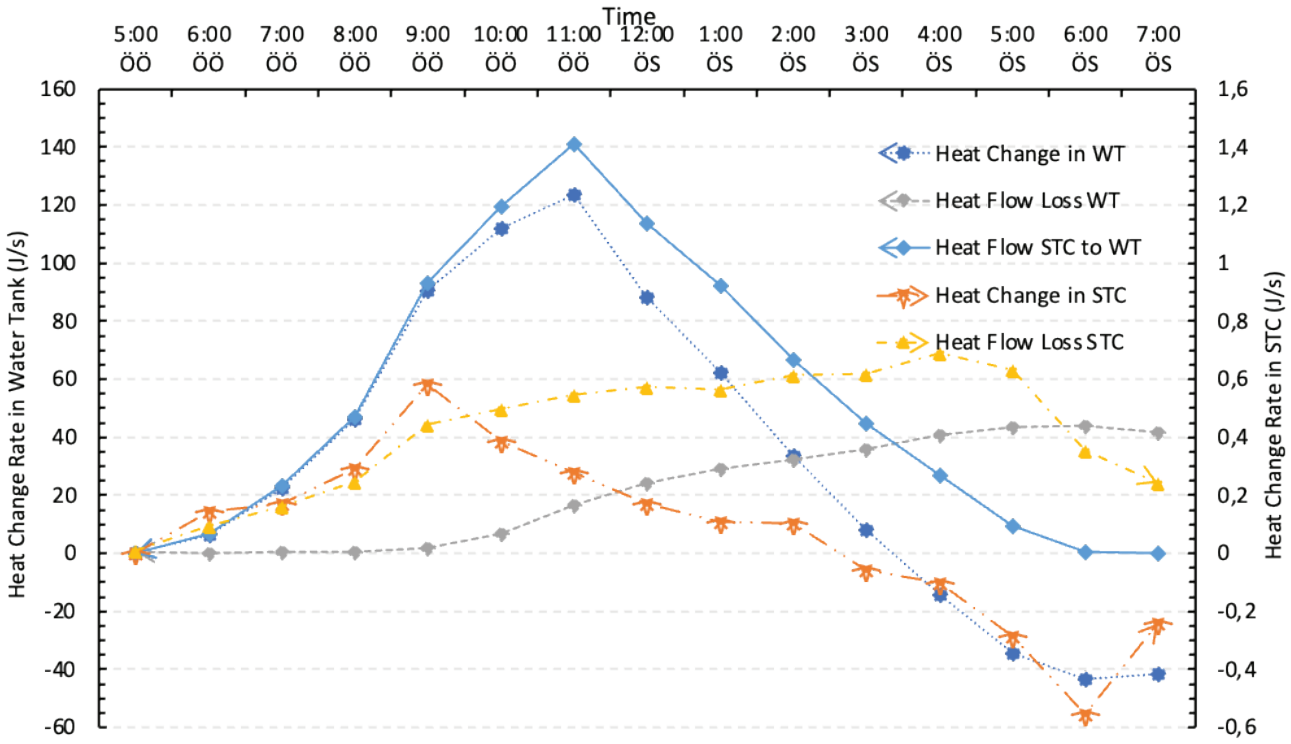

Figure 14. Heat energy flow rate in STC, WT, and STC to WT.

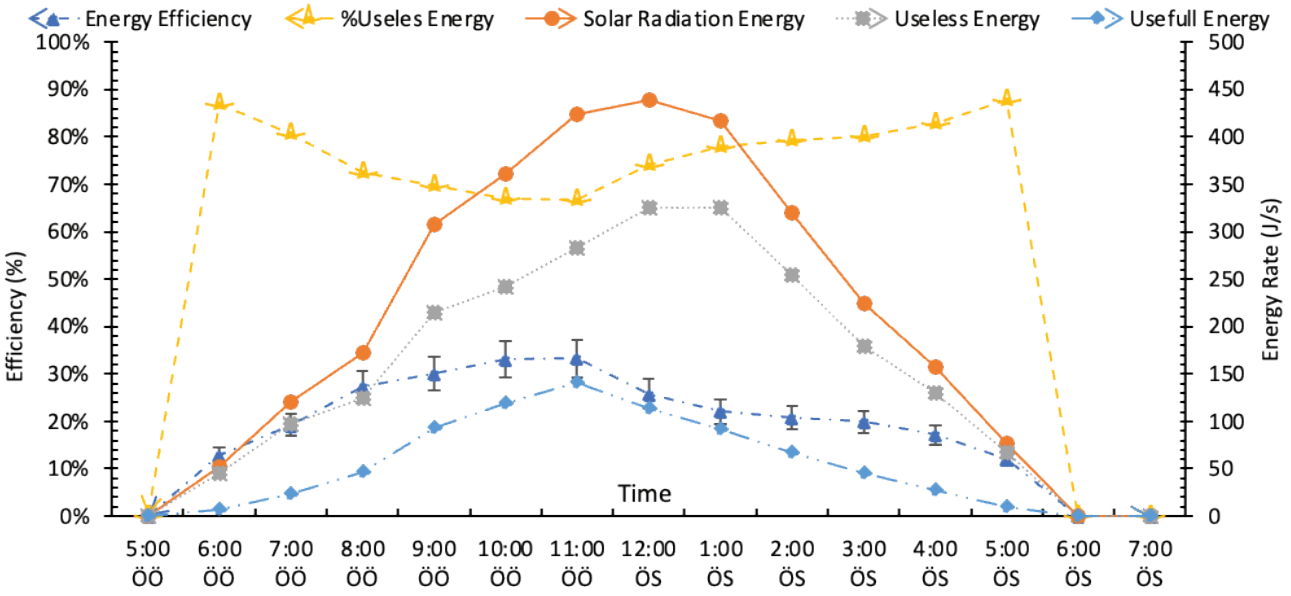

Figure 15. Energy efficiency and energy rate in STC.

efficiency cannot increase anymore because the increase in useless energy continues until 2:00 PM at 87.83%, but the rate of useful energy decreases. The rate of useless energy in percentage increases because the energy conversion efficiency of the photothermal absorber tends to decrease as the light intensity is too low (yellow graph line). However, cumulatively useless energy increases as the intensity of solar radiation entering the system increases (grey graph line). The average STC energy efficiency is 22.84%, and the average useless energy contribution is 77.16%.

Figure 16 and Figure 16 shows that exergy increases drastically as the mass flow rate increases. The mass flow rate will flow faster if the temperature difference is more significant. In the thermosiphon mechanism, the fluid flows faster due to the difference in the density of the water being higher, where a higher temperature will reduce the density and flow upwards. This finding aligns with research conducted by Bhakta and Singh using a parabolic concentrating solar water heater where a drastic increase in mass flow rate resulted in an instant rise in energy efficiency [81, 82].

Figure 17 shows that the highest exergy efficiency was achieved at 11:00 AM at 5.51%, and the average was 3.44%. Furthermore, the highest SI was 1.06, with an average of 1.04. At 5.00 AM and 6.00 PM to 7.00 PM, the SI value is 0, indicating there is no exergy flow to activate the system.

The exergy efficiency of this novel STC shows better performance than that of collector tubes without combination. Ataee and Ameri (2023) reported in their review research that the exergy efficiency of evacuated tubes is limited to 2.3–2.45%. This is because the collector combination increases the focus value of the light, thereby increasing the temperature generation. Higher outlet temperature has a positive impact on STC exergy. Conversely, higher inlet and ambient temperatures have a negative impact on STC exergy.

Energy and exergy efficiency of SWH

Figure 18 shows that the average contribution of unsaved energy dominates at 79.08%, influenced by useless energy at 75.03%. Therefore, the average energy efficiency that can be stored is only 20.92%. In addition, the heat loss contribution increases more rapidly with increasing time compared to the cumulative heat energy in the tank, which

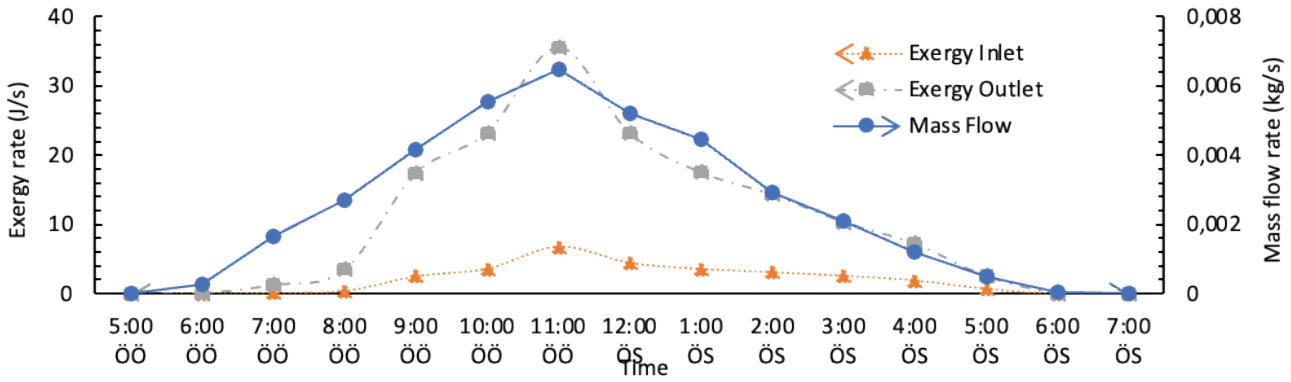

Figure 16. Exergy of STC and mass flow rate.

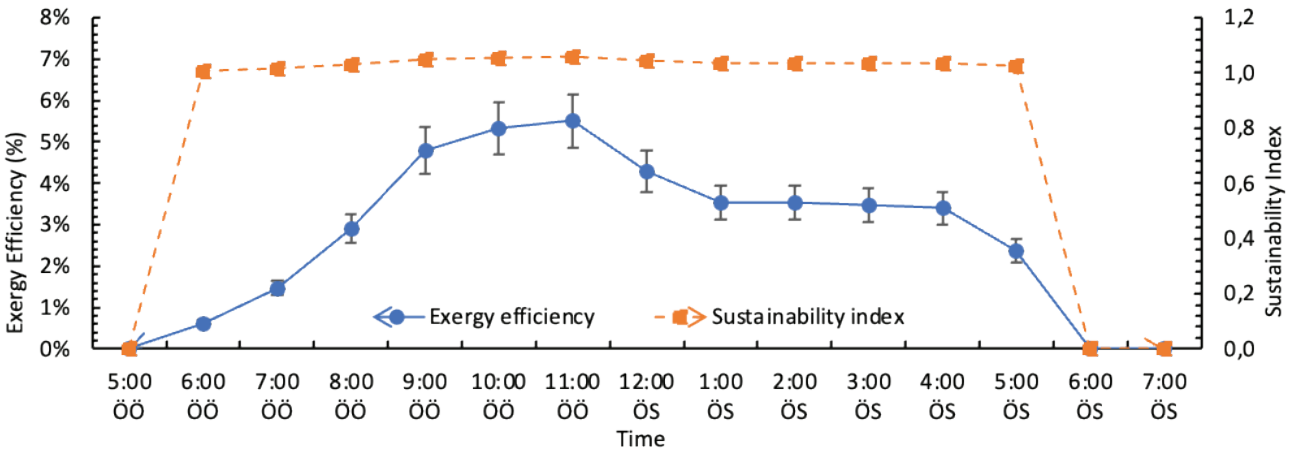

Figure 17. Exergy efficiency and sustainability of STC.

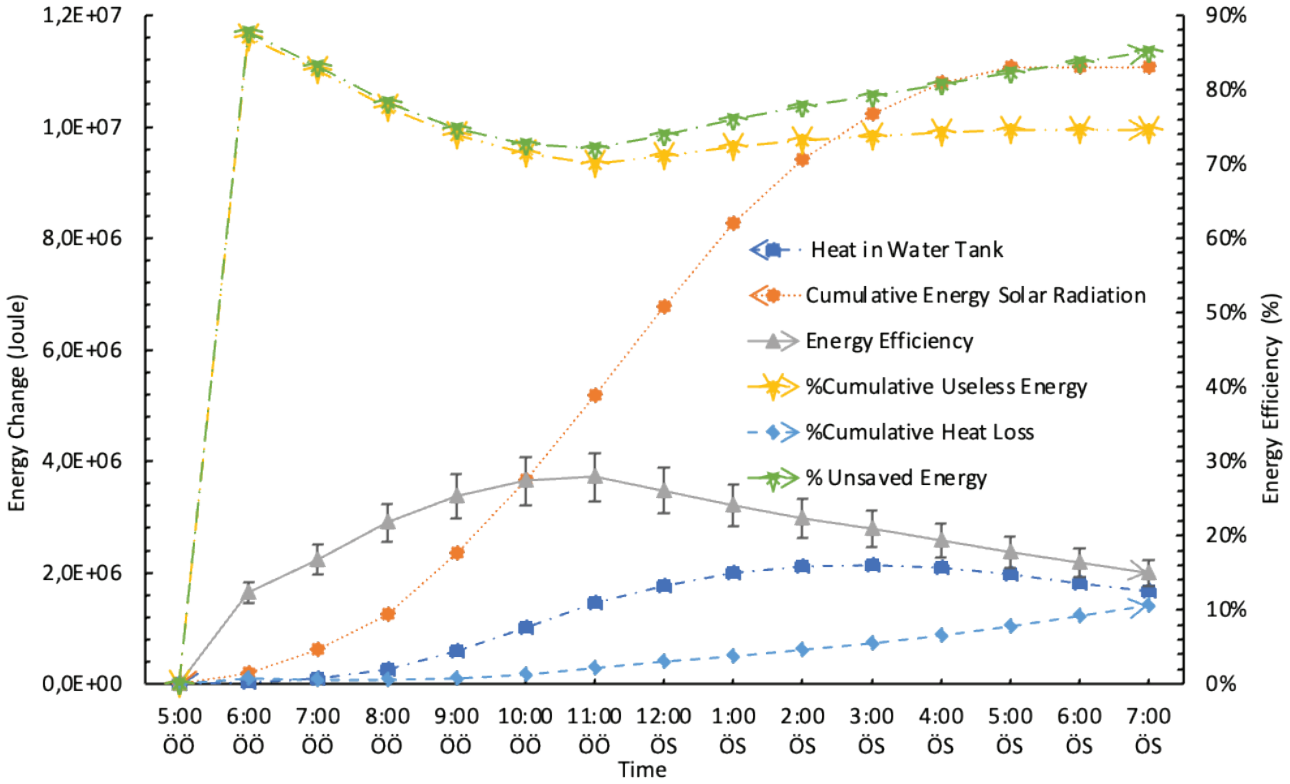

Figure 18. Energy change and energy efficiency of SWH.

decreases SWH efficiency since 3:00 PM. The exergy input in Figure 19 follows the trend of exergy cumulative solar radiation trend input in Figure 18. This indicates that the exergy input is predominantly influenced by the cumulative solar radiation energy.

The exergy input to the SWH increases in the morning along with the increase in solar radiation, peaking in the afternoon before stabilizing, while the exergy outcome peaks early in the afternoon and then decreases even though the exergy input is still high, as shown in Figure 19. The continuous increase in tank temperature causes faster heat dissipation and decreases the energy conversion efficiency, as shown in Figure 18. Meanwhile, the ambient temperature also increases until noon before starting to decrease in the afternoon. This condition contributes to the decrease in exergy outcome because the temperature difference between the working fluid and the environment becomes smaller. Therefore, the potential energy that can be converted decreases. This trend follows the findings of Hasan et al. (2018), which showed that increasing ambient temperature can reduce the exergy in the SWH system. In addition, although the cumulative energy from radiation continues to increase, the decrease in solar radiation in the afternoon further limits the increase in exergy outcome, indicating that the

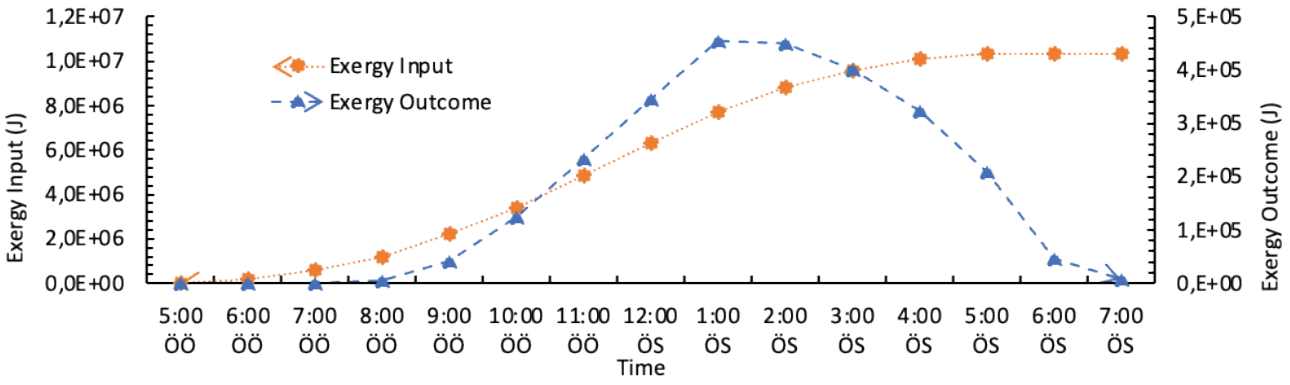

Figure 19. Exergy input and outcome in STC.

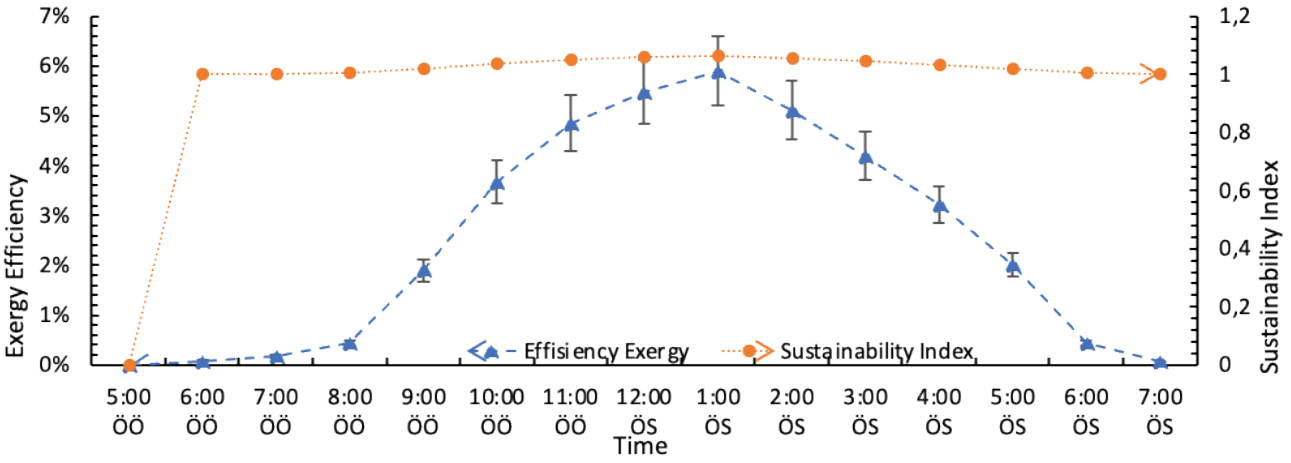

Figure 20. Exergy Efficiency and Sustainability Index SWH.

thermal dynamics and solar radiation greatly influence the system performance throughout the day.

The average and highest exergy efficiency, shown in Figure 20, is 3.09% and 5.90%. Furthermore, the average and highest sustainability index is 1.032 and 1.063. Exergy outcome and SI SWH at 6:00 PM to 7:00 PM are not yet worth 0 because there is still exergy stored. However, it will continue to experience exergy loss due to heat loss. Eventually, the outcome exergy and SI SWH values will become 0 if the water storage temperature is the same as the initial temperature.

Uncertainty of Measurement and Performance

Table 6 shows that the solar and xenon lamp radiation parameters have higher uncertainty conditions of more than 1%. These results are reasonable because the uncertainty in testing under sunlight can reach 15% to 60% on

Table 6. Uncertainty of measurement

Parameter and Performance	Symbol	Unit	$\%\overline{\text{CoV}}$
Xenon radiation	$\bar{G}_{xenon}$	W/m²	7.07%
T ambient control condition	$\bar{T}_{ambient.25\pm1K}$	K	0.35%
Absorber temperature generation under Xenon illumination mesh 5-10	$\bar{T}_{abs.50-10.xenon}$	K	0.11%
Absorber temperature generation under Xenon illumination mesh 10-20	$\bar{T}_{abs.10-20.xenon}$	K	0.09%
Absorber temperature generation under Xenon illumination mesh 20-60	$\bar{T}_{abs.20-60.xenon}$	K	0.09%
Absorber temperature generation under Xenon illumination mesh 60-100	$\bar{T}_{abs.60-100.xenon}$	K	0.08%
Solar radiation unloaded test (15-17 Agustus 2023)	$\bar{G}_{solar.ul}$	W/m²	8.18%
Absorber T1 unloaded test	$\bar{T}_{1.ul}$	K	0.29%
Absorber T2 unloaded test	$\bar{T}_{2.ul}$	K	0.32%
Absorber T3 unloaded test	$\bar{T}_{3.ul}$	K	0.37%
Average Absorber T unloaded test	$\bar{\bar{T}}_{ul}$	K	6.43%
Temperature of ambient	$\bar{T}_{ambient.l}$	K	0.35%
Solar radiation loaded test (12-14 Agustus 2023)	$\bar{G}_{solar.l}$	W/m²	11.67%
Temperature of collector inlet	$\bar{T}_{in.col}$	K	0.26%
Temperature of collector outlet	$\bar{T}_{out.col}$	K	0.13%
Temperature of water tank	$\bar{T}_{wt}$	K	0.15%
Temperature of ambient	$\bar{T}_{ambient.l}$	K	0.16%

Table 7. Calculated performance uncertainty due to error propagation

Key Performance	δ_I
Energy Efficiency of Absorbers	6.586%
Exergy Efficiency of Absorber	6.605%
Energy Efficiency of STC	11.709%
Exergy Efficiency of STC	11.713%
Energy Efficiency of SWH	11.709%
Exergy Efficiency of SWH	11.710%

cloudy days and 2% -40% on sunny days [83]. High measurement uncertainty in solar radiation is caused by changes in natural conditions that cannot be controlled. Meanwhile, sources of uncertainty in xenon lamp radiation are unstable electricity, dust, shocks, measuring instruments, lamp quality, and instrument setup. However, the ambient temperature parameters have low uncertainty conditions. These different parameter conditions can still result in low measurement uncertainty for most performance. Only the average temperature generation performance at three test points without loading produces high measurement uncertainty conditions. This condition occurs because the focus of the lens moves due to changes in the angle of solar radiation, which indicates that the temperature at the absorber is uneven and hot spots are moving. However, no research has examined the maximum limit of parameter uncertainty to consider the reliability data of photothermal absorbers, STC, and SWH technology performance.

The uncertainty value due to error propagation for each calculated performance is classified as high because it is more than 1%, as presented in Table 7. The uncertainty in error propagation in this test is high due to the high uncertainty in the solar radiation intensity. Meanwhile, measurement uncertainty for other performances has a small impact on calculated performance error propagation because the value is less than 1%.

CONCLUSION

This study comprehensively examines the performance of granular coal photothermal absorber in the novel design of a solar thermal collector, a combination of Fresnel lens-compound parabolic reflector, applied to solar water heater. Based on experimental data and comprehensive analysis, it is concluded that:

- Granular coal photothermal absorber has a light trap structure, that is, the gap between granules' contact, fracture porosity, and rough surfaces.
- The main composition of granular coal photothermal absorber is carbon and oxygen , with minority elements niobium , iron , and aluminum.
- The temperature generation test using a xenon lamp and the absorbance test using spectrophotometry found that granular coal photothermal absorber size 10 to 20 was the best.
- The ideal operational limit of granular coal photothermal absorber in the oxidation stage region, at a temperature of 336.31 K to 684.31 K, with a maximum mass change of 11.95%.
- In the unloaded condition test (real environment test using solar thermal collector), the maximum generation absorber temperature was 399.25 K, with an energy conversion efficiency of 86% and an exergy efficiency of 21.29%.
- In loaded condition testing (real environment test using solar water heater), it was found that the optimal temperature of the solar thermal collector outlet and water in the solar water heater storage was 317.88 K and 316.75 K.
- The stored water temperature performance has met the ideal for warm bathing.
- The maximum solar thermal collector energy efficiency is 33.06%, and the average is 22.90%, while the maximum exergy efficiency is 5.51%, and the average is 3.44%.
- The maximum solar water heater energy efficiency is 27.85%, and the average is 20%, while the maximum solar water heater exergy efficiency is 5.90%, and the average is 3.09%.

LIMITATIONS AND FUTURE IMPROVEMENTS

This study shows that granular coal has good potential as a photothermal absorber in thermal solar collectors, especially for low to medium temperature applications. This material can absorb heat well, but some aspects can still be further developed. One of the main challenges is to improve efficiency and exergy. Furthermore, expanding the operational temperature range allows this technology to be applied in various applications. In addition, although material properties such as size, shape, type, and absorbance are known to affect temperature and heat performance, this relationship has not been formulated mathematically with high accuracy. Further studies are also needed to evaluate the material's durability in long-term use and analyze the economic aspects in commercial-scale applications.

In the future, innovation is needed in the development of absorber materials with higher thermal stability and longer durability so that the efficiency and service life of the system can be improved. More innovative collector designs, such as integrating tracking and geometry engineering, can potentially significantly improve energy the efficiency of energy and exergy. In addition, exploring combinations of other photothermal materials can help improve overall system performance. The application of more complex numerical models and computational simulations is also needed to formulate the mathematical relationship between

material properties and performance. This approach can improve the accuracy of predicting collector performance under various environmental conditions. Therefore, this technology can be applied more widely and effectively.

AUTHORSHIP CONTRIBUTIONS

Authors equally contributed to this work.

DATA AVAILABILITY STATEMENT

The authors confirm that the data that supports the findings of this study are available within the article. Raw data that support the finding of this study are available from the corresponding author, upon reasonable request.

CONFLICT OF INTEREST

The author declared no potential conflicts of interest with respect to the research, authorship, and/or publication of this article.

ETHICS

There are no ethical issues with the publication of this manuscript.

STATEMENT ON THE USE OF ARTIFICIAL INTELLIGENCE

Artificial intelligence was not used in the preparation of the article.

REFERENCES

[1] IEA, "Energy Statistics Data Browser," iea.org. Available at: https://www.iea.org/data-and-statistics/data-tools/energy-statistics-data-browser?country=WORLD&fuel=Energy supply&indicator=TESbySource Accessed Dec 25, 2024.

[2] Vojáček O, Brabec J, Macháč J. Costs of achieving emission limits in coal-burning power plants under the recent best available techniques regulation amendment: Evidence from national microeconomic data J Clean Prod 2022;352:131600. [Crossref]

[3] Zhang Z, Zhao Z, Zhang L. Recent progress in the gasification reaction behavior of coal char under unconventional combustion modes. Appl Therm Eng 2023;220:119742. [Crossref]

[4] NASA. The Balance of Power in the Earth-Sun System 2005. Available: https://eospso.nasa.gov/sites/default/files/publications/NASA-Facts-EnergyBalance.pdf. Accesed on March 2, 2026.

[5] Our World in Data, "Power Generation and Cumulative Capacity of Solar Energy," ourworldindata.org. Available: https://ourworldindata.org/grapher/solar-energy-consumption-by-region?tab=table&time=earliest..2023 Accessed on Sept. 02, 2023.

[6] Energy Institute, "Statistical Review of World Energy Data," energyinst.org. Available at: https://www.energyinst.org/statistical-review/resources-and-data-downloads. Accesed on March 02, 2026.

[7] He W, Zhou L, Wang M, Cao Y, Chen X, Hou Xç Structure development of carbon-based solar-driven water evaporation systems. Sci Bull 2021;66:1472–1483. [Crossref]

[8] Sarifudin A, Yaningsih I, Kristiawan B, Ubaidillah. Recent Material Research Advances for Photothermal Absorbers. Evergreen 2024;11:2035–2062. [Crossref]

[9] Sarifudin A. A comprehensive review of granular structures as photothermal absorber materials. Therm Sci Eng Prog 2024;14:102689. [Crossref]

[10] Kanimozhi B, Nitin shinde Y, Paul Bedford S, Swaroop Kanth K, Vikash Kumar S. Experimental Analysis of Solar Water Heater Using Porous Medium with Agitator. Mater Today Proc vol. 2019;16:1204–1211. [Crossref]

[11] Wirawan M, Mirmanto M, Fahrurrozi I. The Influence of the Tilt Angle of a Flat Plate Solar Collector with Granite Stone Absorber on Its Performance. Int J Adv Eng Manag 2023;5:1234–1238.

[12] Ternenge Abur B, Dandakouta H, Ejilah RI, Adisa AB. Modeling and Simulation of an Indirect Natural Convection Solar Dryer with Thermal Storage Bed. Int J Eng Manuf v. 2020;10:24–42. [Crossref]

[13] Li J, Jing Y, Zhou X, Mao J. Multifunctional photothermal materials based on natural pumices for high efficiency <scp>solar-driven</scp> interface evaporator. Int J Energy Res 2021;45:20132–20142. [Crossref]

[14] Bilal A, Jamil B, Haque NU, Ansari MA. Investigating the effect of pumice stones sensible heat storage on the performance of a solar still. Groundw Sustain Dev 2019;9:100228. [Crossref]

[15] Attia MEH, Kabeel AE, Abdelgaied M. Optimal concentration of El Oued sand grains as energy storage materials for enhancement of hemispherical distillers performance. J Energy Storage 2021;36. [Crossref]

[16] Elashmawy M. Improving the performance of a parabolic concentrator solar tracking-tubular solar still (PCST-TSS) using gravel as a sensible heat storage material. Desalination 2020;473: 114182. [Crossref]

[17] López-Sosa LB, Ortíz-Carrión A, Espinosa-Gómez D, Zárate Medina J, González-Avilés M, Solar air heating system with low environmental impact materials: Mathematical model and optothermal characterization. Sustain Energy Technol Assessments 2021;47:101399. [Crossref]

[18] Elmaadawy K, Kandeal AW, Khalil A, Elkadeem MR, Liu B, Sharshir SW. Performance improvement of double slope solar still via combinations of low cost materials integrated with glass cooling. Desalination 2021;500:114856. [Crossref]

[19] Mohamed AF, Hegazi AA, Sultan GI, El-Said EMS. Enhancement of a solar still performance by inclusion the basalt stones as a porous sensible absorber: Experimental study and thermo-economic analysis. Sol Energy Mater Sol Cells 2019;200:109958. [Crossref]

[20] Arunkumar T, Wang J, Dsilva Winfred Rufuss D, Denkenberger D, Kabeel AE. Sensible desalting: Investigation of sensible thermal storage materials in solar stills. J Energy Storage 2020;32:101824. [Crossref]

[21] Sarifudin A, Yaningsih I, Kristiawan B. Solar Thermal Technology First Elec Yogyakarta: Propublikasi Republik Indonesia, 2024. Available at: https://propublikasi.com/buku/pb00001/. Accessed on: March 2, 2026.

[22] Bie Y, Li Z, Lei J, Ma Z, Li M, Krolczyk G, et al. Solar medium-low temperature thermal utilization and effect analysis of boundary condition: A tutorial. Sol Energy 2020;197:238–253. [Crossref]

[23] Barone G, Buonomano A, Forzano C, Palombo A. Solar thermal collectors. Sol Hydrog Prod Process Syst Technol 2019;151–178. [Crossref]

[24] Farjana SH, Huda N, Mahmud MAP, Saidur R. Solar process heat in industrial systems – A global review. Renew Sustain Energy Rev 2018;82:2270–2286. [Crossref]

[25] Sarifudin A, Yaningssih I, Kristiawan B, Wibawa A. Investigation of Granular Natural Stone Materials as Photothermal Absorbers for Sustainable and Environmentally Friendly Energy Harvesting. J Appl Eng Sci 2024;22:1–16. [Crossref]

[26] Sarifudin A, Yaningsih I, Kristiawan B, Miyazaki T, Thu K. Temperature Generation of Granular Photothermal Absorber Natural Materials Using Fresnel Lens Collector. In: Salim MA, Khashi NS, Chew KW, Photong C, editors. Proceedings of the 9th International Conference and Exhibition on Sustainable Energy and Advanced Materials. 2024. 313–317. [Crossref]

[27] Chamsa-ard W, Brundavanam S, Fung C, Fawcett D, Poinern G. Nanofluid Types, Their Synthesis, Properties and Incorporation in Direct Solar Thermal Collectors: A Review. Nanomaterials 2017;7:131.

[28] Kalogirou SA. Solar thermal collectors and applications. Prog Energy Combust Sci 2004;30:231–295. [Crossref]

[29] Jensen AR, Sifnaios I, Caringal GP, Furbo S, Dragsted J. Thermal performance assessment of the world's first solar thermal Fresnel lens collector field. Sol Energy 2022. [Crossref]

[30] Sarafraz MM, Tlili I, Tian Z, Bakouri M, Safaei MR. Smart optimization of a thermosyphon heat pipe for an evacuated tube solar collector using response surface methodology (RSM). Phys A Stat Mech its Appl 2019;534:122146. [Crossref]

[31] Sharma MK, Bhattacharya J. Dependence of spectral factor on angle of incidence for monocrystalline silicon based photovoltaic solar panel. Renew Energy 2022;184:820–829. [Crossref]

[32] Pu J, Shen C, Yang S,. Zhang C,. Chwieduk D, Kalogirou SA. Feasibility investigation on using silver nanorods in energy saving windows for light/heat decoupling. Energy 2022;245: 123289. [Crossref]

[33] Gupta VK, Kumar S, Kukreja R, Chander N. Experimental thermal performance investigation of a direct absorption solar collector using hybrid nanofluid of gold nanoparticles with natural extract of Azadirachta Indica leaves. Renew Energy 2023;202:1021–1031. [Crossref]

[34] Gao M, Zhu L, Peh CK, Ho GW. Solar absorber material and system designs for photothermal water vaporization towards clean water and energy production. Energy Environ Sci 2019;12: 841–864. [Crossref]

[35] Dwivedi KK, Prabhansu MK Karmakar, Chatterjee PK. Thermal degradation, characterization and kinetic modeling of different particle size coal through TGA. Therm Sci Eng Prog 2020; 18:100523. [Crossref]

[36] Yan D, Li M.Stearic acid-modified MOF-based composite phase change materials for solar-thermal energy conversion and storage. Sol Energy 2023;262:111843. [Crossref]

[37] Coccia G, Aquilanti A, Tomassetti S, Ishibashi A, Nicola G Di. Design, manufacture and test of a low-cost solar cooker with high-performance light-concentrating lens. Sol Energy 2021; 224:1028–1039. [Crossref]

[38] Hu T, Kwan TH, Yang H, Wu L. Photothermal conversion potential of full-band solar spectrum based on beam splitting technology in concentrated solar thermal utilization. Energy 2023;268:126763. [Crossref]

[39] Petela R. Exergy of undiluted thermal radiation. Sol Energy 2003;74:469–488. [Crossref]

[40] Milanese M, Colangelo G, de Risi A. Development of a High-Flux Solar Simulator for Experimental Testing of High-Temperature Applications. Energies 2021;14:3124. [Crossref]

[41] A. Interrante. Layers of the Sun, NASA. Available: https://blogs.nasa.gov/sunspot/2023/09/26/layers-of-the-sun/ Accessed on: Oct 08, 2023.

[42] Agrawal A, Kumar A, Parekh AD.Experimental investigation of atmospheric air to water generation based on both end open evacuated tube collector solar air heater. Sol Energy 2023; 263:111953. [Crossref]

[43] Arslan E. Applying regression techniques to determine mathematical equations of exergy, electricity, and energy values of photovoltaic thermal collector. Sol Energy 2023;255:369–380. [Crossref]

[44] Ozbas E, Selimli S, Ozkaymak M, Frej A. Evaluation of internal structure modifications effect of two-phase closed thermosyphon on performance: An experimental study. Sol Energy 2021; 224:1326–1332. [Crossref]
[45] Tuncer AD, Amini A, Khanlari A. Developing an infrared-assisted solar drying system using a vertical solar air heater with perforated baffles and nano-enhanced black paint. *Sol Energy* 2023;263. [Crossref]
[46] Hasan MF, Mahadi MSUR, Miyazaki T, Koyama S, Thu K. Exergy analysis of serpentine thermosyphon solar water heater. Appl Sci 2018;8. [Crossref]
[47] Al-Askaree EH, Al-Muhsen NFO. Experimental investigation on thermal performance of solar water heater equipped with Serpentine fin core heat exchanger. Clean Eng Technol 2023;12: 100593. [Crossref]
[48] Vivas-Cortez M, Fleitas A, Guzmán PM, Nápoles JE, Rosales JJ.Newton's Law of Cooling with Generalized Conformable Derivatives. Symmetry (Basel) 2021;13:1093. [Crossref]
[49] Kabeel AE, Harby K, Abdelgaied M, Eisa A. Performance improvement of a tubular solar still using V-corrugated absorber with wick materials: Numerical and experimental investigations," Sol Energy 2021;217:187–199. [Crossref]
[50] Afshari F, Tuncer AD, Sözen A, Çiftçi E, Khanlari A. Experimental and numerical analysis of a compact indirect solar dehumidification system. 2021. [Crossref]
[51] Ghazouani M, Bouya M, Benaissa M. Thermo-economic and exergy analysis and optimization of small PTC collectors for solar heat integration in industrial processes. Renew Energy 2020;152:984–998. [Crossref]
[52] Mugi VR, Chandramohan VP. Energy and exergy analysis of forced and natural convection indirect solar dryers: Estimation of exergy inflow, outflow, losses, exergy efficiencies and sustainability indicators from drying experiments. J Clean Prod 2021;282:124421. [Crossref]
[53] Yang M, Zhi L, Diao K, Zhu Y, Taylor RA. Optical and thermal performance analysis of a compact solar collector with heat-pipe evacuated tube. Sol Energy 2022; 258:118–129. [Crossref]
[54] Guimarães Barbosa E, Eduardo Viana de Araujo M, Zhang Y, Arêdes Martins M. Exergetic, enviro-economic and exergoeconomic (3E) assessment of a stationary parabolic trough solar collector with thermal storage. Sol Energy 2023;255:487–496. [Crossref]
[55] Selimefendigil F, Şirin C, Ghachem K, Kolsi L. Exergy and environmental analysis of an active greenhouse dryer with Al2O3 nano-embedded latent heat thermal storage system: An experimental study. Appl Therm Eng 2022;217:119167. [Crossref]
[56] Singh OK. Development of a solar cooking system suitable for indoor cooking and its exergy and enviroeconomic analyses. Sol Energy 2021;217:223–234. [Crossref]
[57] Abi Mathew A, Thangavel V. A novel thermal storage integrated evacuated tube heat pipe solar air heater: Energy, exergy, economic and environmental impact analysis. Sol Energy 2021;220:828–842. [Crossref]
[58] Hachchadi O, Tapsoba G, Dery P, Mechaqrane A, Meloche P, Izquierdo R. Experimental optimization of the heating element for a direct-coupled solar photovoltaic water heater. Sol Energy 2023;264:112037. [Crossref]
[59] Jing P, Zhou X, Xu Z, Xu Z. Numerical and Experimental Investigation on Photothermal Performance of Polyimide/High-Electrical-Performance-Coating Composite Films Considering Surface Roughness. J Therm Sci 2022;31:1206–1219. [Crossref]
[60] Çimen M, Colakoglu M, Güngör A. Overheating limitation of thermosiphon solar collectors by controlling heat pipe fluid in all glass evacuated tubes. Sol Energy 2021;230:515–527. [Crossref]
[61] Eltawil MA, Algonaian AA, Amer BMA. Innovative extraction process for date fruits syrup (Dibs) using electro-thermal solar energy. Sol Energy 2020;221:521–535. [Crossref]
[62] Kabeel AE, Diab MR, Elazab MA, El-Said EMS. Solar powered hybrid desalination system using a novel evaporative humidification tower: Experimental investigation Sol Energy Mater Sol Cells 2022;248:112012. [Crossref]
[63] Jeter SM. Maximum conversion efficiency for the utilization of direct solar radiation. Sol Energy 1981;26:231–236. [Crossref]
[64] Gitan AA, Al-Kayiem HH. Assessment of hybrid solar-thermal multi-chamber dryer integrated with desiccant dehumidifier for uniform drying. Sol Energy 2023;262:111880. [Crossref]
[65] Hassan H, Osman OO, Abdelmoez MN, abo-Elfadl S. Experimental assessment of novel designed solar hot water storage collector incorporating an array of partitioned ducts absorber. Sol Energy 2023;262:111838. [Crossref]
[66] Ihoume I, Tadili R, Arboui N, Bazgaou A, Idrissi A, Benchrifa M, Fatnassi H. Performance study of a sustainable solar heating system based on a copper coil water to air heat exchanger for greenhouse heating. 2021;232:128–138. [Crossref]
[67] Schmelzer C, Georgii MJ, Vajen OK. Accuracy of key performance indicators in solar-assisted heating systems due to measurement uncertainties. Sol Energy 2023;249:255–267. [Crossref]
[68] Zhao W, Xiao L, Cui Z, Fang J, Zhang C, Li X et al. Moth-eye-inspired texturing surfaces enabled self-cleaning aluminum to achieve photothermal anti-icing. Opt Laser Technol 2021; 141:107115. [Crossref]

[69] Tang Y, Zhao X, Li D, Zuo X, Tang A, Yang H. Nanoporous carbon-enabled composite phase change materials with high photo-thermal conversion performance for multi-function coating. Sol Energy Mater Sol Cells 2022; 248:112025. [Crossref]

[70] Tuncer AD, Badali Y, Khanlari A. Application of carbon-based nanomaterials in solar-thermal systems: An updated review. Sol Energy 2024; 282:112932. [Crossref]

[71] Zhao S, Zhang Y. DFT study on the chemisorption and reforming of naphthalene over bio-char: The detailed mechanism of carbon deposition and hydrogen production. Fuel 2023; 332: 126144. [Crossref]

[72] Dai S, Finkelman RB, French D, Hower JC, Graham IT, Zhao F. Modes of occurrence of elements in coal: A critical evaluation. Earth-Science Rev 2021;222:103815. [Crossref]

[73] Attia MEH, Kabeel AE, Abdelgaied M, Abdel-Aziz MM, Bellila A, Abdullah A. Optimal size of black gravel as energy storage materials for performance improvement of hemispherical distillers. J Energy Storage 2021; 43:103196. [Crossref]

[74] Chen M, He Y, Zhu J, Kim DR. Enhancement of photo-thermal conversion using gold nanofluids with different particle sizes. Energy Convers Manag 2016;112:21–30. [Crossref]

[75] Zhu W, Zuo X, Ding Y, Yan H, An Y, Yang W. Experimental investigation on the photothermal conversion performance of cuttlefish ink nanofluids for direct absorption solar collectors. Appl Therm Eng 2023; 221:119835. [Crossref]

[76] Kumar Mohalik N, Mandal S, Kumar Ray S, Mobin Khan A, Mishra D, Krishna Pandey J. TGA/DSC study to characterise and classify coal seams conforming to susceptibility towards spontaneous combustion. Int J Min Sci Technol 2022; 32:75–88. [Crossref]

[77] Mandal S, Mohalik NK, Ray SK, Khan AM, Mishra D, Pandey JK. A comparative kinetic study between TGA & DSC techniques using model-free and model-based analyses to assess spontaneous combustion propensity of Indian coals. Process Saf Environ Prot 2022; 159: 1113–1126. [Crossref]

[78] Kellali S, Richard F, Batiot B, Cremona P, Rogaume T. Modelling of lignite pyrolysis using a finite rate chemistry approach: comparison between parallel and competitive chemical schemes. J Anal Appl Pyrolysis 2023;172:105975. [Crossref]

[79] Yanbolagh DJ, Saraei A, Mazaheri H, Mehrabadi SJ. Exergoeconomic, Environmental, Economic, and Energy-Matrices (4E) Analysis of Three Solar Distillation Systems Equipped with Condenser and Different Heaters. J Therm Eng 2021;7:1640–1653. [Crossref]

[80] Sousa V, Meireles I. Dynamic simulation of the energy consumption and carbon emissions for domestic hot water production in a touristic region. J Clean Prod 2022; 355:131828. [Crossref]

[81] Bhakta AK, Singh SN. Thermo-Hydraulic Performance Analysis of Parabolic Concentrating Solar Water Heater. J Therm Eng 2020; 6:802–815. [Crossref]

[82] Ataee S, Ameri M. Energy and exergy parameter analysis of a U-pipe evacuated tubular solar collector with filled and unfilled layer. Appl Therm Eng 2023; 233:121190. [Crossref]

[83] Biencinto M, González L, Valenzuela L. Using time-windowed solar radiation profiles to assess the daily uncertainty of solar thermal electricity production forecasts J Clean Prod 2022; 379:134821. [Crossref]